# A single hole spin with enhanced coherence in natural silicon

N. Piot,[1,*] B. Brun,[1,*] V. Schmitt,[1] S. Zihlmann,[1] V. P. Michal,[2] A. Apra,[1] J. C. Abadillo-Uriel,[2] X. Jehl,[1] B. Bertrand,[3] H. Niebojewski,[3] L. Hutin,[3] M. Vinet,[3] M. Urdampilleta,[4] T. Meunier,[4] Y.-M. Niquet,[2] R. Maurand,[1,†] and S. De Franceschi[1,‡]

[1] *Univ. Grenoble Alpes, CEA, Grenoble INP, IRIG-Pheliqs, Grenoble, France.*
[2] *Univ. Grenoble Alpes, CEA, Grenoble INP, IRIG-MEM-L_Sim, Grenoble, France.*
[3] *Univ. Grenoble Alpes, CEA, LETI, Minatec Campus, Grenoble, France.*
[4] *Univ. Grenoble Alpes, CNRS, Grenoble INP, Institut Néel, Grenoble, France.*

(Dated: January 24, 2022)

**Semiconductor spin qubits based on spin-orbit states are responsive to electric field excitation allowing for practical, fast and potentially scalable qubit control. Spin-electric susceptibility, however, renders these qubits generally vulnerable to electrical noise, which limits their coherence time. Here we report on a spin-orbit qubit consisting of a single hole electrostatically confined in a natural silicon metal-oxide-semiconductor device. By varying the magnetic field orientation, we reveal the existence of operation sweet spots where the impact of charge noise is minimized while preserving an efficient electric-dipole spin control. We correspondingly observe an extension of the Hahn-echo coherence time up to 88 $\mu$s, exceeding by an order of magnitude the best reported values for hole-spin qubits, and approaching the state-of-the-art for electron spin qubits with synthetic spin-orbit coupling in isotopically-purified silicon. This finding largely enhances the prospects of silicon-based hole spin qubits for scalable quantum information processing.**

## INTRODUCTION

In the global effort to build scalable quantum processors, spin qubits in semiconductor quantum dots[1] are progressively making their mark[2]. We highlight, in particular, the achievement of single-[3,4] and two-qubit[5–8] gate fidelities well above 99%, the first realizations of multi-qubit arrays[9,10], and a demonstrated compatibility with industrial-grade semiconductor manufacturing technologies[11–13].

Owing to their long coherence time, electron-spin qubits in silicon quantum dots have so far attracted the largest attention[2]. That said, their control requires add-ons such as metal microstrips[3], micromagnets[4], or dielectric resonators[14], whose large-scale integration is technically challenging[13]. Hole-spin qubits, on the other hand, can circumvent this difficulty thanks to their intrinsically large spin-orbit coupling, which enables electric-dipole spin manipulation. Over the last five years a variety of hole spin qubits have been reported in both silicon[11,15] and germanium[16–19] quantum dots. In all these qubits, quantum operations are performed using high-frequency gate voltage excitations.

The downside of all-electrical spin control is that the required spin-orbit coupling exposes the qubit to charge noise, leading to a reduced hole spin coherence. Recent theoretical works[20,21], however, have shown that, for properly chosen structural geometries and magnetic field orientations, careful tuning of the electrostatic confinement can bring the hole qubit to an optimal operation point where the effects of charge noise vanish to first order while enabling efficient electric-dipole spin resonance. Here, using a single hole spin confined in natural silicon we pinpoint the existence of operation sweet-spots where the longitudinal spin-electric susceptibility is minimized, resulting in a large enhancement of the spin coherence time.

## DEVICE AND $g$-FACTORS

Our device consists of an undoped silicon nanowire with rectangular cross-section whose electrostatics is controlled by four gates (G1 to G4) as shown in Figs. 1a,b (see Methods for details). We define a large hole island below G3 and G4 to be used simultaneously as a Fermi reservoir and as a charge sensor for a single hole trapped in a quantum dot,

* Contributed equally to the work.
† romain.maurand@cea.fr
‡ silvano.defranceschi@cea.fr

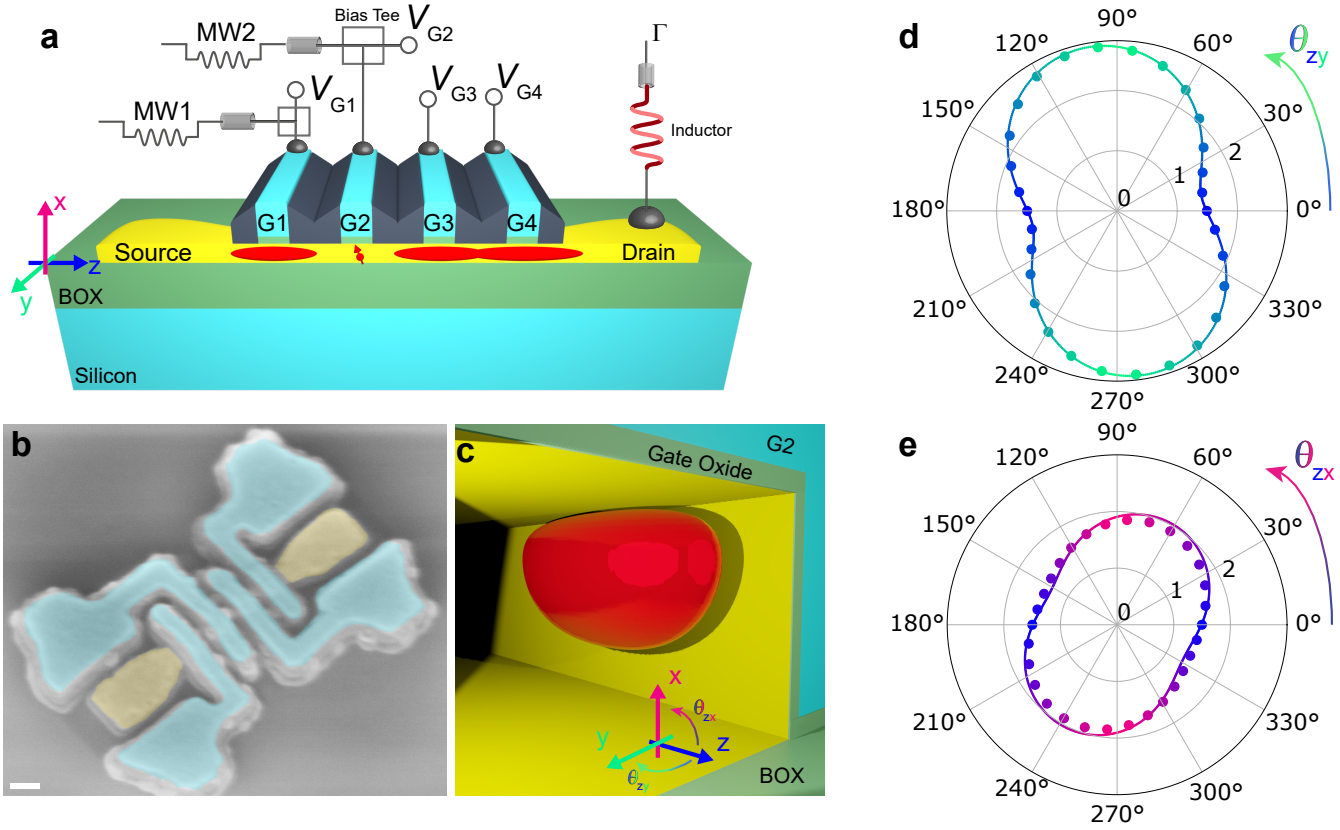


FIG. 1. **Device, measurement scheme, and properties of the first confined hole.** **(a)** Simplified 3-dimensional representation of a silicon (yellow)-on-insulator (green) nanowire device with four gates (light blue) labelled G1, G2, G3 and G4. Gate G2 defines a quantum dot (QD2) hosting a single hole; G3 and G4 define a hole island used as reservoir and sensor for hole spin readout; G1 defines a hole island screening QD2 from dopant disorder and fluctuations in the source. Using bias-tees, both static voltages ($V_{G1}$, $V_{G2}$) and time-dependent, high-frequency voltages (MW1, MW2) can be applied to G1 and G2, respectively. The drain contact is connected to an off-chip, surface-mount inductor to enable rf reflectometry readout. The coordinate system used for the magnetic field is shown on the left side. Each axis is given a different color, which is used throughout the manuscript to indicate the magnetic field orientation. **(b)** Colorized scanning electron micrograph showing a tilted view of a device similar to the measured one. Image taken just after the etching of the spacer layers. Scale bar: 100 nm **(c)** Artistic view of the computed wave function for the first hole accumulated under G2. The red iso-density surface encloses 85% of the probability of presence of the hole. **(d)** Measured (dots) and calculated (solid line) hole $g$-factor as a function of the in-plane magnetic field angle $\theta_{zy}$ (dots). $\theta_{zy} = 90°$ corresponds to a magnetic field applied along the $y$ axis. **(e)** Same as (d) in the $xz$ plane. $\theta_{zx} = 90°$ corresponds to a magnetic field applied along the $x$ axis.

QD2, under G2. Single-shot readout of this hole spin is performed by means of a spin-to-charge conversion technique based on the real-time detection of spin-selective tunneling to the Fermi reservoir, a widely used method often referred to as "Elzerman readout"[22]. Tunneling events are detected by dispersive rf-reflectometry on the charge sensor (see Methods and Supp. Info S1 for technical details).

In our device geometry, the first holes primarily accumulate in the upper corners of the Si nanowire[23]. Figure 1c displays the expected single hole wave function in QD2, computed with a finite-differences $\mathbf{k} \cdot \mathbf{p}$ model including the six topmost valence bands[24] (see Supp. Info S2). At low-energy, i.e. close to the valence-band edge, the hole wave function primarily contains heavy-hole (HH) and light-hole (LH) components. The strong two-axes confinement readily seen in Fig. 1c favors HH-LH mixing[25,26]. This mixing is expected to manifest in the anisotropy of the hole $g$-tensor, which bears information on the relative weight of HH and LH components[27–29]. To verify this, we measure the hole spin resonance frequency $f_L$ while varying the orientation of the magnetic field $\mathbf{B}$ in the $xz$ and $yz$ planes. The effective $g$-factor $g = hf_L/(\mu_B|\mathbf{B}|)$ (with $\mu_B$ the Bohr magneton and $h$ the Planck constant) is plotted in Figs. 1d and 1e as a function of the magnetic field angles $\theta_{zx}$ and $\theta_{zy}$, respectively. These maps highlight the strong anisotropy of the Zeeman splitting, with a maximal $g = 2.7$ close to the $y$ axis (in-plane, perpendicular to the wire) and a minimal $g = 1.4$ close the $z$ axis (in-plane, along the wire). The calculated $g$-factors are also plotted in the same figures as colored solid lines. The agreement with the experimental data is remarkable. From the numerical simulation, we

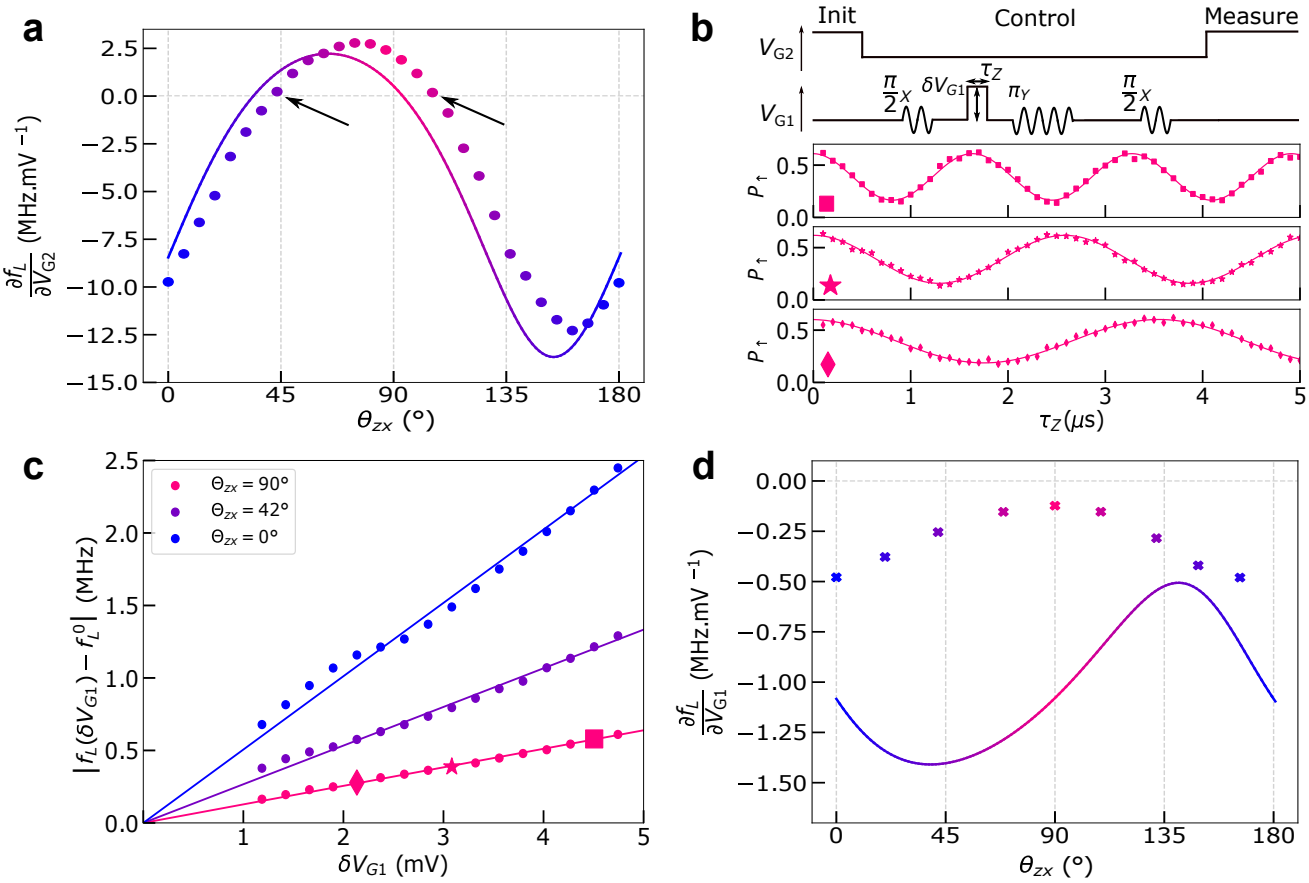


FIG. 2. **Longitudinal spin-electric susceptibility (LSES). (a)** Spin-electric susceptibility with respect to $V_{G2}$ ($\mathrm{LSES_{G2}}$) as a function of magnetic field angle $\theta_{zx}$ (symbols), at constant $f_L = 19\,\mathrm{GHz}$. The LSES vanishes at $\theta_{zx} = 41°$ and 106°, as indicated by the two arrows. The solid line corresponds to the numerically calculated $\mathrm{LSES_{G2}}$. **(b)** (top) Pulse sequence used to measure $\mathrm{LSES_{G1}}$: a voltage pulse of amplitude $\delta V_{G1}$ and duration $\tau_Z$ is applied to G1 during the first free evolution time of a Hahn-echo sequence. (bottom) Spin-up fraction $P_\uparrow$ as a function of $\tau_Z$ for $\delta V_{G1} = 2.16\,\mathrm{mV}$ (diamonds), 3.12 mV (stars) and 4.80 mV (squares), at $\theta_{zx} = 90°$. The oscillation frequency varies with $\delta V_{G1}$. **(c)** $\delta V_{G1}$ dependence of the frequency shift extracted from the Hahn-echo measurements at $\theta_{zx} = 0°$, 42° and 90°. Symbols in the latter data set correspond to the $P_\uparrow$ oscillations shown in (b). The solid lines are linear fits to the experimental data whose slope directly yields $|\mathrm{LSES_{G1}}|$. **(d)** Measured (symbols) and calculated (solid line) $\mathrm{LSES_{G1}}$ as a function of $\theta_{zx}$, at constant $f_L = 17\,\mathrm{GHz}$. The negative sign of $\mathrm{LSES_{G1}}$ is inferred from the shift of $f_L$ under a change in $V_{G1}$.

conclude that the measured $g$-factor anisotropy results from a strong electrical confinement against the side facet of the channel (along $y$), which prevails over the mostly structural vertical confinement (along $x$). The experimental $g$-factors and the small misalignment between the principal axes of the $g$-tensor and the device symmetry axes are best reproduced by introducing a moderate amount of charge disorder in combination with small ($\sim 0.1\%$) shear strains in the silicon channel (see Supp. Info S2). The latter likely originate from device processing and thermal contraction at the measurement temperature[30].

## LONGITUDINAL SPIN-ELECTRIC SUSCEPTIBILITY

Given that the $g$-factor anisotropy is intimately related to the HH/LH mixing, which is controlled by the electrostatic confinement potential, the Larmor frequency is expected to be gate-voltage dependent. As a consequence, the hole spin coherence must be generally susceptible to charge noise. We thus measure the longitudinal spin-electric susceptibility (LSES) with respect to the voltages applied to the lateral gate G1 and to the accumulation gate G2, which we define as $\mathrm{LSES_{G1}} = \dfrac{\partial f_L}{\partial V_{G1}}$ and $\mathrm{LSES_{G2}} = \dfrac{\partial f_L}{\partial V_{G2}}$, respectively. In essence, $\mathrm{LSES_{G1}}$ and $\mathrm{LSES_{G2}}$ characterize the response of the Larmor frequency to the electric-field components parallel ($z$) and perpendicular ($x, y$) to the channel direction,

respectively.

To probe the response to G2, we directly measure the spin resonance frequency $f_L$ at different $V_{G2}$ (see Supp. Info S3 for details). The resulting $\mathrm{LSES}_{G2}$ is plotted as a function of the magnetic field angle $\theta_{zx}$ in Fig. 2a. The observed angular dependence is in good agreement with the theoretical expectation.

Noticeably, $\mathrm{LSES}_{G2}$ is positive along $x$ and negative along $z$. Indeed, when increasing $V_{G2}$, the hole wave function extends proportionally more in the $yz$ plane than in the vertical $x$ direction, which increases $g_x$ and decreases $g_y$ and $g_z$ (see Supp. Info S2). As a result of the sign change, $\mathrm{LSES}_{G2}$ vanishes at two magnetic field orientations in the $xz$ plane (marked by arrows in Fig. 2a), which are sweet-spots for electric-field fluctuations perpendicular to the silicon channel.

To probe the response to G1, we introduce a pulse on $V_{G1}$ in a Hahn-echo sequence[4] as outlined in Fig. 2b. This defines a phase gate, controlled by the amplitude $\delta V_{G1}$ and duration $\tau_Z$ of the pulse. Figure 2b displays the coherent oscillations recorded as a function of $\tau_Z$ for three different pulse amplitudes. The frequency of these oscillations is expected to increase linearly with $\delta V_{G1}$, with a slope $\mathrm{LSES}_{G1} = \frac{\partial f_L}{\partial V_{G1}}$. This is shown in Fig. 2c for different magnetic field orientations. $\mathrm{LSES}_{G1}$, plotted in Fig. 2d as a function of $\theta_{zx}$, ranges from $-0.5\,\mathrm{MHz/mV}$ to $-0.1\,\mathrm{MHz/mV}$. Its magnitude is much smaller than $\mathrm{LSES}_{G2}$ because G1 is farther from QD2 than G2 and its field effect is partly screened by the hole gas beneath. The numerically calculated $\mathrm{LSES}_{G1}$ (solid line) reproduces reasonably well the order of magnitude but not the angular dependence of the measured $\mathrm{LSES}_{G1}$. This discrepancy is likely due to the unknown charge disorder in the spacer layers between the gates (see discussion in Supp. Info S2). We also notice that $\mathrm{LSES}_{G1}$ never vanishes and that the minimum of $|\mathrm{LSES}_{G1}|$ happens to be almost at the same $\theta_{zx}$ as a zero of $\mathrm{LSES}_{G2}$.

## COHERENCE TIMES

We now turn to the angular dependence of the hole spin coherence time and investigate its correlation with the longitudinal spin-electric susceptibility[31]. To get rid of low frequency noise sources, we measure the coherence time using a conventional Hahn-echo protocol[2]. The control sequence, applied to G1 (see upper inset of Fig. 3a), consists of $\pi_x/2$, $\pi_y$ and $\pi_\phi/2$ pulses separated by a time delay $\tau_{\mathrm{wait}}/2$. For each $\tau_{\mathrm{wait}}$, we extract the averaged amplitude of the $P_\uparrow$ oscillation obtained by varying the phase $\phi$ of the last $\pi/2$ pulse, and normalize it to the $P_\uparrow$ oscillation amplitude in the zero-delay limit. A representative Hahn-echo plot is shown in Fig. 3a. We fit the echo amplitude to an exponential decay $\exp(-(\tau_{\mathrm{wait}}/T_2^{\mathrm{E}})^\beta)$, where the exponent $\beta$ is left as a free parameter. The best fit is obtained for $\beta = 1.5 \pm 0.1$, which implies a high frequency noise with a characteristic spectrum $S(f) = S_{\mathrm{hf}}(f_0/f)^\alpha$, where $f_0 = 1\,\mathrm{Hz}$ is a reference frequency and $\alpha = \beta - 1 \approx 0.5$ (we note that the same $\alpha$ value was reported for hole spin qubits in germanium[10]).

To explore the angular dependence of $T_2^{\mathrm{E}}$ in the $xz$ plane, we measure the decay of the Hahn-echo amplitude for different values of $\theta_{zx}$. The results, shown in Fig. 3b, reveal a strong anisotropy, with $T_2^{\mathrm{E}}$ ranging from $15\,\mu\mathrm{s}$ to $88\,\mu\mathrm{s}$. Strikingly, the spin coherence time peaks at $\theta_{zx} = 99°$, an angle between the minimum of $|\mathrm{LSES}_{G1}|$ and a zero of $\mathrm{LSES}_{G2}$, highlighting a correlation with the correspondingly suppressed electrical noise. The extended coherence time is much longer than previously reported for hole spin qubits in both silicon and germanium[32]. In addition, we notice that spin control remains efficient at all angles including $\theta_{zx} = 99°$, where we could readily achieve Rabi frequencies as high as 5 MHz limited by the attenuation on the microwave line (see Supp. Info S4).

The observed angular dependence of $T_2^{\mathrm{E}}$ can be understood by assuming that the electrical noise is the sum of uncorrelated voltage fluctuations on the different gates G$i$ with respective spectral densities $S_{Gi}(f) = S_{Gi}^{\mathrm{hf}}(f_0/f)^{0.5}$. Given the Hahn-Echo noise filter function, the decoherence rate can then be expressed as (see Supp. Info S5):

$$\frac{1}{T_2^{\mathrm{E}}} \approx 7.8 f_0^{1/3} \left( \sum_i \left( \frac{\partial f_L}{\partial V_{Gi}} \right)^2 S_{Gi}^{\mathrm{hf}} \right)^{2/3} . \tag{1}$$

Using the longitudinal spin-electric susceptibilities from Figs. 2a and 2d and leaving the weights $S_{Gi}^{\mathrm{hf}}$ as adjustable parameters, we achieve a remarkable agreement with the experimental $T_2^{\mathrm{E}}$ (see colored solid line in Fig. 3b). This strongly supports the hypothesis that the Hahn-echo coherence time is limited by electrical noise. As already argued before, $\mathrm{LSES}_{G1}$ and $\mathrm{LSES}_{G2}$ indeed quantify the susceptibility of the hole spin to electric field fluctuations parallel and perpendicular to the channel, respectively.

The best fit in Fig. 3b is obtained with $S_{G1}^{\mathrm{hf}} = (2.6\,\mu\mathrm{V}/\sqrt{\mathrm{Hz}})^2$ and $S_{G2}^{\mathrm{hf}} = (0.1\,\mu\mathrm{V}/\sqrt{\mathrm{Hz}})^2$. We speculate that the large $S_{G1}^{\mathrm{hf}}/S_{G2}^{\mathrm{hf}}$ ratio results from an artificial enhancement of $S_{G1}^{\mathrm{hf}}$ accounting for hidden sources of electric field fluctuations along the silicon nanowire. Certainly, Eq. (1) misses the contribution from the electrical noise on G3, whose LSES could not be measured. For a symmetry reason, we expect $\mathrm{LSES}_{G3}$ to be comparable to $\mathrm{LSES}_{G1}$. A

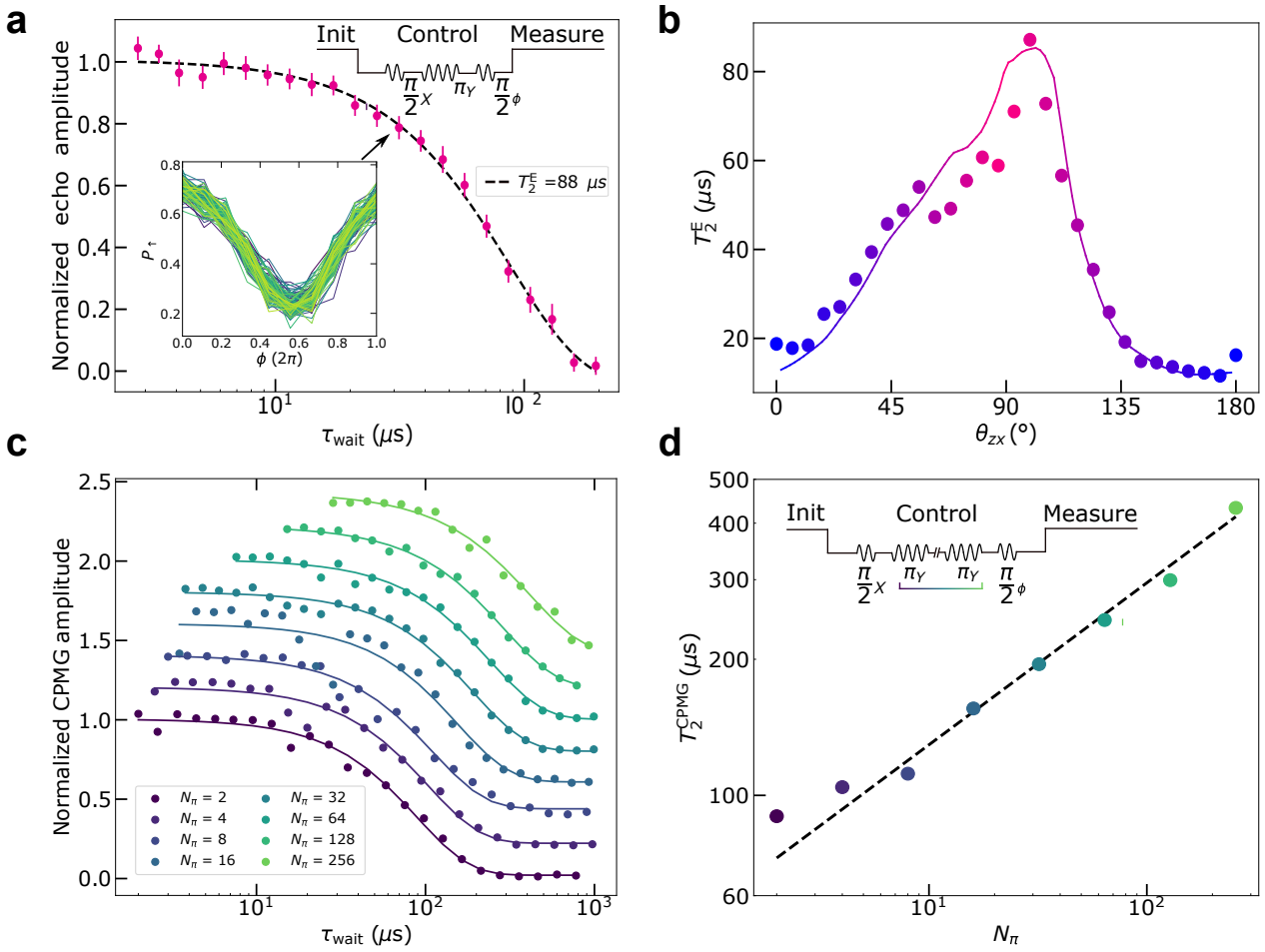


FIG. 3. **Anisotropy of the hole spin coherence and sweet-spot operation. (a)** Normalized Hahn-echo amplitude *vs* free evolution time $\tau_{\rm wait}$ at $f_L = 17\,$GHz. The top-right inset sketches the pulse sequence. The down-left inset displays $P_\uparrow(\tau_{\rm wait} = 31.4\,\mu{\rm s})$ *vs* the phase $\phi$ of the last $\pi/2$ pulse for 100 repetitions. For each $\tau_{\rm wait}$, we extract the average amplitude of the $P_\uparrow(\phi)$ oscillations and normalize it to the average amplitude in the zero-delay limit. The resulting normalized echo amplitudes are reported on the main plot. The dashed curve is a fit to $\exp(-(\tau_{\rm wait}/T_2^E)^\beta)$ with $\beta = 1.5 \pm 0.1$. **(b)** Measured $T_2^{\rm E}$ vs magnetic field angle $\theta_{zx}$ (symbols). The solid line is a fit to Eq. (1), using the experimental $\rm LSES_{G1}$ and $\rm LSES_{G2}$ from Figs. 2a and 2d. **(c)** Normalized CPMG amplitude as a function of free evolution time $\tau_{\rm wait}$ for different numbers $N_\pi$ of $\pi$ pulses (curves are offset for clarity). The solid lines are fits to the same exponential decay function as in (a) with $\beta = 1.5$. **(d)** Extracted $T_2^{\rm CPMG}$ as a function of $N_\pi$. The dashed line is a linear fit with slope $\gamma = 0.33$. The inset sketches the CPMG pulse sequence: $N_\pi$ equally spaced $\pi_y$ pulses between two $\pi_x/2$ pulses. As for Hahn-echo, we detune the phase of the last pulse.

possible additional source of longitudinal electric field fluctuations is the randomly oscillating charges and dipoles in the silicon nitride spacers between the gates. They presumably make a large contribution to the apparent $S_{\rm G1}^{\rm hf}$ as they are closer to QD2 and less screened by the hole gas than gate G1 itself.

To further investigate the hole spin coherence, we implemente Carr–Purcell–Meiboom–Gill (CPMG) sequences at the most favorable field orientation $\theta_{zx} = 99°$. These consist in increasing the number of $\pi$ pulses cancelling faster and faster dephasing mechanisms. Figure 3c displays the CPMG echo amplitudes as a function of the total waiting time $\tau_{\rm wait}$ for series of $N_\pi = 2^n$ $\pi$ pulses, where $n$ is an integer ranging from 1 to 8. The CPMG decay times $T_2^{\rm CPMG}$ extracted from Fig. 3c (see caption) are plotted against $N_\pi$ in Fig. 3d. As expected, the data points follow a power law $T_2^{\rm CPMG} \propto N_\pi^\gamma$, where $\gamma = \frac{\alpha}{\alpha+1}$ for a $\propto 1/f^\alpha$ noise spectrum[4]. The best fit value $\gamma = 0.33$ yields again $\alpha = 0.5$. For the largest sequence of 256 $\pi$ pulses, we find $T_2^{\rm CPMG} = 0.4$ ms, which is the longest coherence ever reported for hole spins[32].

Finally, to gain insight into the low frequency noise acting on the hole spin, we perform systematic measurements of the inhomogeneous dephasing time $T_2^*$. To this aim, we apply Ramsey control sequences consisting of two $\pi/2$ pulses separated by a variable delay $\tau_{\rm wait}$. Contrary to Hahn-echo, the dephasing induced by low frequency noise sources

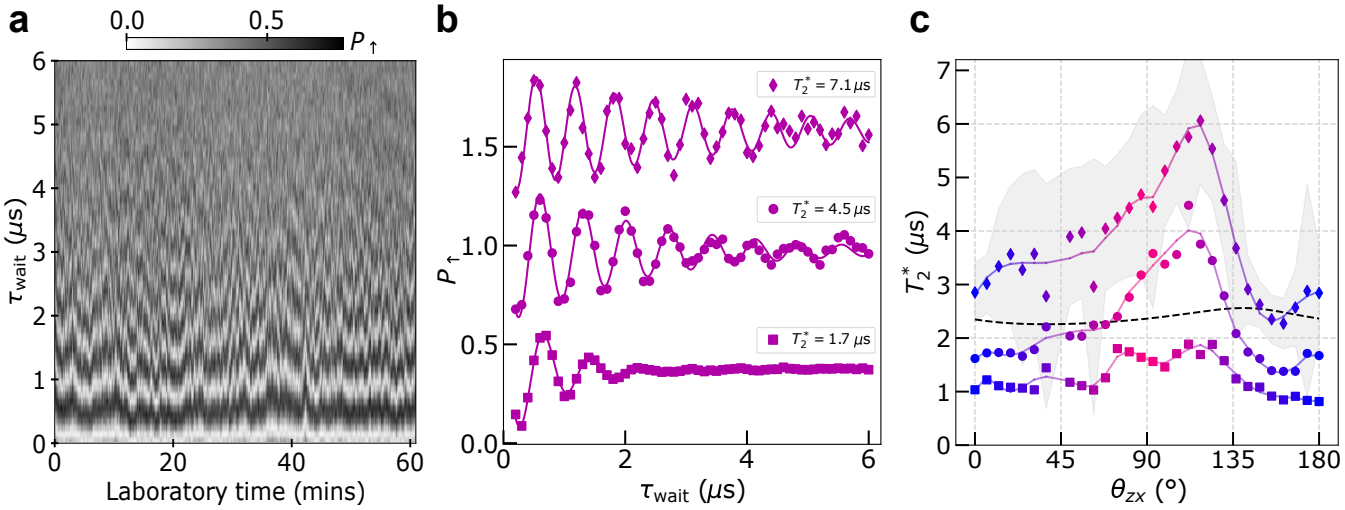


FIG. 4. **Free induction decay (FID). (a)** Collection of 600 Ramsey oscillations as a function of $\tau_{\rm wait}$, the free evolution time between two $\pi_x/2$ pulses, at $\theta_{zx} = 118°$. The applied microwave frequency is detuned by $\sim$ 700 kHz from the Larmor frequency. Each Ramsey oscillation is measured in approximately 5.5 s. **(b)** Selected averages of Ramsey oscillations taken over different measurement times: $t_{\rm meas} = 5.5$ s corresponding to a single trace (diamonds); $t_{\rm meas} = 27.5$ s, corresponding to 5 consecutive traces (circles); $t_{\rm meas} \approx 1$ hour, corresponding to the full set of 600 traces (squares). The solid lines are fits to Gaussian decaying oscillations. **(c)** Average $T_2^*$ versus magnetic field angle $\theta_{zx}$ for the same three $t_{\rm meas}$ as in (b) (same symbol notation). The shaded grey area highlights the standard deviation for $t_{\rm meas} = 5.5$ s, while the solid lines are smooth guides to the eye. Dashed line: calculated dephasing time due to hyperfine interactions (see Supp. Info S7).

is not cancelled due to the absence of the refocusing $\pi$ pulse. Figure 4a displays $P_\uparrow$ for a series of identical Ramsey sequences recorded on an overall time frame of one hour, with each sequence lasting approximately 5.5 s. The next step is to average $P_\uparrow(\tau_{\rm wait})$ on a subset of consecutive sequences measured within a total time $t_{\rm meas}$. This way, an averaged Ramsey oscillation is obtained for each $t_{\rm meas}$, whose amplitude is fitted to a Gaussian-decay function yielding $T_2^*(t_{\rm meas})$. Representative Ramsey data sets and corresponding fits are shown in Fig. 4b for three values of $t_{\rm meas}$. The inhomogeneous dephasing time decreases with increasing $t_{\rm meas}$ due to the contribution of noise components with lower and lower frequency.

To unveil the angular dependence $T_2^*$, we repeat the same measurement protocol for different magnetic field orientations. Figure 4c shows $T_2^*(\theta_{zx})$ for three values of $t_{\rm meas}$. The anisotropy of the Hahn-echo decay time of Fig. 3b can still be identified at the shortest $t_{\rm meas}$, but it gets progressively washed out as $t_{\rm meas}$ is increased.

Moreover, if the $1/f^{0.5}$ charge noise prevailed over the whole mHz to MHz range, $T_2^*$ would be $\approx 50\,\mu$s when $T_2^{\rm E} \approx 88\,\mu$s (see Supp. Info S5), well above the $6\,\mu$s seen in Fig. 4c. The power spectrum $S(f)$ at low frequency can be extracted from the data of Fig. 4a (see Supp. Info S6). This reveals a $1/f^\alpha$ noise with $\alpha$ closer to 1, and a power (at 1 Hz) four orders of magnitude larger than the one expected by extrapolating the high-frequency $1/f^{0.5}$ noise inferred from CPMG. The change of color and amplitude of $S(f)$ when going from the mHz to the MHz points to the presence of different mechanisms dominating the dephasing at low and high frequencies. We note that the $T_2^* \approx 1-2\,\mu$s measured at long $t_{\rm meas}$ is below but fairly close to the expected hole spin dephasing time due to hyperfine interactions with the naturally present $^{29}$Si nuclear spins[23] (see the dashed line in Fig. 4c and Supp. Info S7 for details). This suggests that low-frequency dephasing may be partially due to such hyperfine interactions.

In conclusion, we have reported on the first spin qubit with electrical control and single-shot readout based on a single hole in a silicon nanowire device issued from an industrial-grade fabrication line. The hole wave function and corresponding $g$-factors could be modeled with an unprecedented level of accuracy in these types of devices, denoting a relatively low level of structural and charge disorder. The hole-spin coherence was found to be limited by a $1/f^{0.5}$ charge noise at high frequencies ($10^4 - 10^6$ Hz), with a strong dependence on the magnetic-field orientation that could be faithfully accounted for by the spin-electric susceptibilities. A largely enhanced spin coherence was measured at the sweet-spot angle, far beyond the current state-of-the-art for hole-spin qubits and close to the best reported figures for electron-spin qubits in $^{28}$Si. Our study of the inhomogeneous dephasing time revealed a much stronger noise at low frequencies ($10^{-4} - 10^{-2}$ Hz) which could be partially ascribed to the expected hyperfine interaction. In this scenario, the possible introduction of isotopically purified silicon devices would lead to significant improvement of hole-spin coherence in the low-frequency range.

## Methods

**Device.**

The device is a four-gate silicon-on-insulator nanowire transistor fabricated in an industry-standard 300-mm CMOS platform[11]. The undoped [110]-oriented silicon nanowire channel is 17 nm thick and 100 nm wide. It is connected to wider boron-doped source and drain pads used as reservoirs of holes. The four wrapping gates (G1, G2, G3 and G4) are 40 nm long and they are spaced by 40 nm. The gaps between adjacent gates and between the outer gates and the doped contacts are filled by silicon nitride spacers. The gate stack consists of a 6 nm thick $SiO_2$ dielectric layer followed by a metallic bilayer with 6 nm of TiN and 50 nm of heavily doped poly-silicon. The experimental setup used to measure the device is described in Supp. Info S8.

**Dispersive readout.**

Similar to charge detection methods recently applied to SOI nanowire devices[33,34], we accumulate a large hole island under the gates G3 and G4, as sketched in Fig. 1a. The island acts both as a charge reservoir and electrometer for the quantum dot QD2 located under G2. However, unlike the above-mentioned earlier implementations, the electrometer is sensed by rf dispersive reflectometry on a tank LC resonator connected to the drain rather than to a gate electrode. To this aim, a commercial surface-mount inductor ($L = 240$ nH) is wire bonded to the drain pad (see Supp. Info S8). This configuration involves a parasitic capacitance to ground $C_p = 0.54$ pF, leading to resonance frequency $f = 449.81$ MHz. The high value of the loaded quality factor $Q \approx 10^3$ enables fast, high-fidelity charge sensing. We estimate a charge readout fidelity of 99.6% in 5 $\mu$s, which is close to the state-of-the-art for Si MOS devices[35]. The resonator characteristic frequency experiences a shift at each Coulomb resonance of the hole island, *i.e.* when the electrochemical potential of the island lines up with the drain Fermi energy. This leads to a dispersive shift in the phase $\phi_{\text{drain}}$ of the reflected radio-frequency signal, which is measured through homodyne detection (See Supp. Info S1 for details on the spin readout).

**Pulse sequences.**

For Ramsey, Hahn echo, phase gate and CPMG pulse sequences, we set a $\pi/2$ rotation time of 50 ns. The Rabi frequency being angular dependent, we calibrate the microwave power required for this operation time prior to apply the pulse sequence, for each magnetic field orientation. We also calibrate the amplitude of the $\pi$ pulses to achieve a $\pi$ rotation in 150 ns.

**Data availability.**

All of the data used to produce the figures in this paper and to support our analysis and conclusions are available upon reasonable request to the corresponding author.

## Acknowledgments

This research has been supported by the European Union's Horizon 2020 research and innovation programme under grant agreements No. 951852 (QLSI project), No. 810504 (ERC project QuCube) and No. 759388 (ERC project LONGSPIN), and by the French National Research Agency (ANR) through the projects MAQSi and CMOSQSPIN.

## Authors contributions

N.P. and B.Br. carried out the experiment with help from V.S., S.Z., and A.A. and under the supervision of X.J., R.M. and S.D. V.M, J.C.A.U. and Y.M.N. carried out the theoretical modeling. B.Be, H. N., L.H. and M.V. designed and supervised the fabrication of the device. M.U. and T.M. provided useful comments. N.P., B.Br., Y.M.N., R.M. and S.D co-wrote the papers with input from the other authors.

## Competing financial interests

The authors declare no competing financial interests.

# Supplementary information for "A single hole spin with enhanced coherence in natural silicon"

## S1. ENERGY SELECTIVE SINGLE SHOT READOUT OF SPIN STATE OF THE FIRST HOLE IN QD2

Figure S.1a displays the stability diagram of the device as a function of $V_{G2}$ and $V_{G3}$ when a large quantum dot (acting as a charge sensor) is accumulated under gates G3 and G4. The dashed grey lines outline the charging events in the quantum dot QD2 under G2, detected as discontinuities in the Coulomb peak stripes of the sensor dot. Figure S.1b shows a zoom on the stability diagram around the working point used for single shot spin readout in the main text. The three points labelled Empty (E), Load (L) and Measure (M) are the successive stages of the readout sequence sketched in Fig. S.1c. The quantum dot is initially emptied (E) before loading (L) a hole with a random spin. Both spin states are separated by the Zeeman energy $E_Z = g\mu_B B$ where $g$ is the $g$-factor, $\mu_B$ the Bohr magneton and $B$ the amplitude of the magnetic field. This opens a narrow window for energy selective readout using spin to charge conversion[36]. Namely, we align at stage (M) the center of the Zeeman splitted energy levels in QD2 with the chemical potential of the sensor. In this configuration, only the excited spin up hole can tunnel out of QD2 while only spin down holes from the sensor can tunnel in. These tunneling events are detected by thresholding the phase of the reflectometry signal of the sensor to achieve single shot readout of the spin state. Typical time traces of the reflected signal phase at stage (M), representative of a spin up (spin down) in QD2, are shown in Fig. S.1d.

We used this three stage pulse sequence to optimize the readout. For that purpose, the tunnel rates between QD2 and the charge sensor were adjusted by fine tuning $V_{G3}$ and $V_{G4}$. For the spin manipulation experiment discussed in the main text, we used a simplified two stages sequence for readout by removing the empty stage. The measure stage duration was set to 200 $\mu$s for all experiments, while the load stage duration (seen as a manipulation stage duration) was ranging from 50 $\mu$s to 1 ms. In order to obtain the spin-up probability $P_\uparrow$ after a given spin manipulation sequence, we repeated the single-shot readout a large number of times, typically 100 to 1000 times.

## S2. MODELING OF THE $g$-FACTORS

### A. Methodology

The device (Fig. S.2) is modeled as a [110]-oriented rectangular nanowire channel with width $W = 100$ nm and height $H = 17$ nm lying on a 145 nm thick buried oxide (BOX). Four 40 nm long and 50 nm tall front gates, separated by 40 nm long $Si_3N_4$ spacers, are laid across the channel. They are insulated by a 6 nm thick $SiO_2$ layer. Highly doped source and drain reservoirs ($N_A = 10^{20}$ cm$^{-3}$) are overgrown at both ends of the channel. The whole device is embedded in a 35 nm thick $Si_3N_4$ contact etch stop layer (CESL), and coated with a $\simeq 250$ nm thick oxide. The silicon substrate beneath can be used as a back gate, and a wide metal line above (at the Metal 1 level) as an extra top gate. These top and back gates, as well as the source and drain are grounded in the simulations.

The potential landscape $V(\mathbf{r})$ in the device is first computed with a finite volumes Poisson solver[24]. Screening by the holes accumulated in the source, drain and below the gates G1, G3, and G4 is accounted for in the Thomas-Fermi approximation. Namely, these accumulations are modeled as locally homogeneous 3D hole gases, with density:

$$p(\mathbf{r}) = N_v F_{1/2}\left[\beta\left(E_v - eV(\mathbf{r}) - \mu\right)\right], \tag{1}$$

where $F_{1/2}$ is a Fermi-Dirac integral, $N_v = (3.5\times10^{15}\,\mathrm{cm^{-3}.K^{-3/2}})T^{3/2}$ is the effective density of states in the valence band, $E_v - \mu$ is difference between the valence band edge energy and the chemical potential (chosen to match the threshold voltage of the device), and $\beta = 1/k_BT$ with $T$ the temperature. This equation is solved self-consistently together with Poisson's equation:

$$\varepsilon_0\nabla\varepsilon_r(\mathbf{r})\cdot\nabla V(\mathbf{r}) = -e\left[p(\mathbf{r}) + \rho_{\mathrm{test}}(\mathbf{r}) + \rho_{\mathrm{trap}}(\mathbf{r}) - N_A(\mathbf{r})\right], \tag{2}$$

where $\varepsilon_0\varepsilon_r(\mathbf{r})$ is the material-dependent dielectric constant, $\rho_{\mathrm{test}}(\mathbf{r})$ is a test charge distribution that mimics a single hole within the dot QD2 under G2, and $\rho_{\mathrm{trap}}(\mathbf{r})$ is a distribution of charge traps used to assess the effects of disorder. The test charge $\rho_{\mathrm{test}}(\mathbf{r})$ prevents the Thomas-Fermi density from flooding the dot, as this approximation is notoriously inaccurate in the few holes regime. The bias voltages are used to set the boundary conditions on the gates.

The test charge distribution $\rho_{\mathrm{test}}(\mathbf{r})$ is practically modeled as a homogeneous ellipsoid with total charge +1, centered on the average position $\mathbf{R} = (\langle x\rangle, \langle y\rangle, \langle z\rangle)$ of the hole (computed *a posteriori* from the quantum-mechanical wave functions), with radii $a_x = \sqrt{3(\langle x^2\rangle - \langle x\rangle^2)}$, $a_y = \sqrt{3(\langle y^2\rangle - \langle y\rangle^2)}$, and $a_z = \sqrt{3(\langle z^2\rangle - \langle z\rangle^2)}$. As the potential $V_{\mathrm{QD}}(\mathbf{r})$ relevant for the Hamiltonian of the dot is that of the empty QD2, the self-consistent $V(\mathbf{r})$ is corrected from the contribution of $\rho_{\mathrm{test}}(\mathbf{r})$:

$$V_{\mathrm{QD}}(\mathbf{r}) = V(\mathbf{r}) - V_{\mathrm{test}}(\mathbf{r}), \tag{3}$$

where $V_{\mathrm{test}}(\mathbf{r})$ is the potential created by $\rho_{\mathrm{test}}(\mathbf{r})$:

$$\varepsilon_0\nabla\varepsilon_r(\mathbf{r})\cdot\nabla V_{\mathrm{test}}(\mathbf{r}) = -e\rho_{\mathrm{test}}(\mathbf{r}). \tag{4}$$

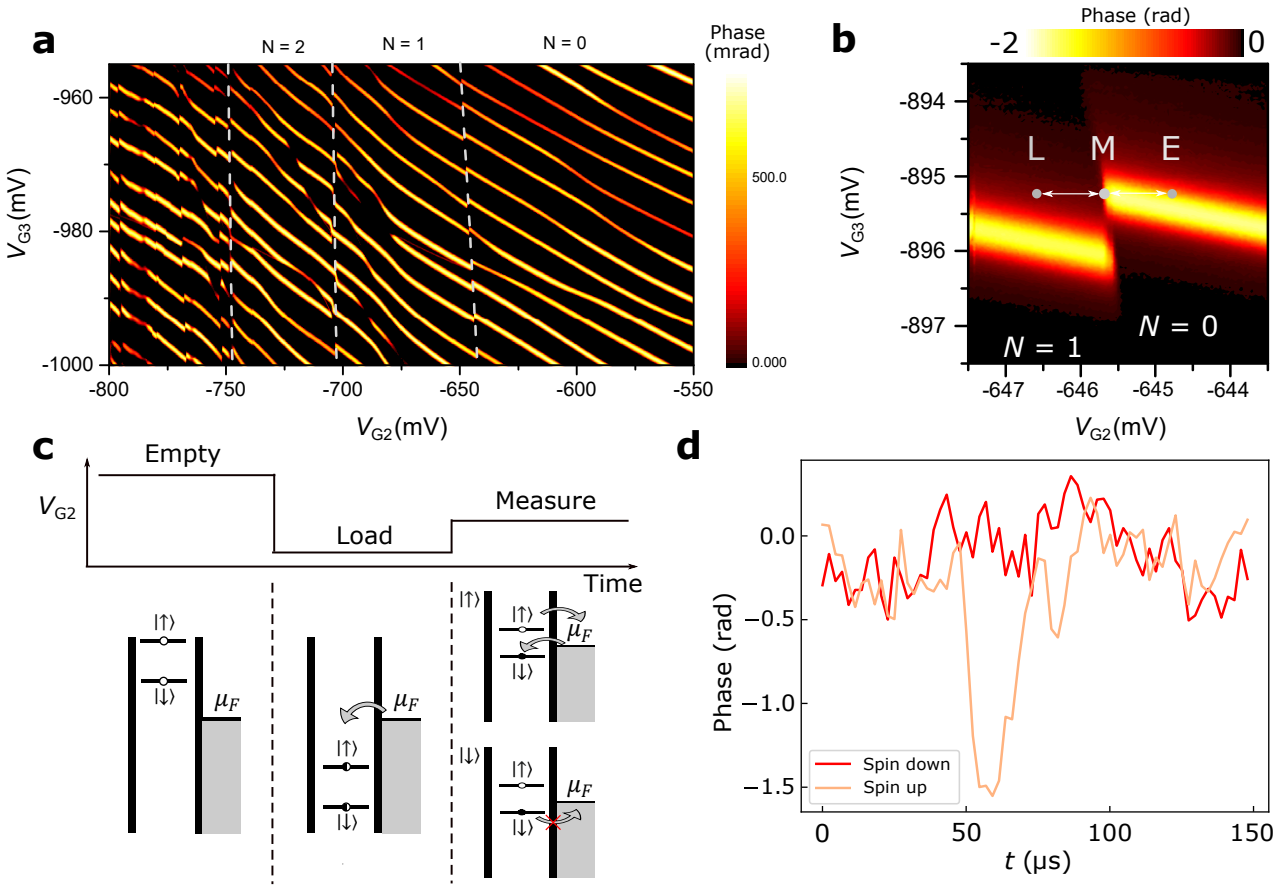


FIG. S.1. **Single shot spin readout. (a)** Stability diagram of the device as a function of $V_{G2}$ and $V_{G3}$. The dashed grey lines are guides to the eye highlighting charge transitions in QD2. The first hole tunnels into QD2 at $V_{G2} \approx -650\,\text{mV}$. **(b)** Zoom on the stability diagram close to the working point used in the main text. The points labelled L (Load), M (Measure) and E (Empty) are the three stages of the pulse sequence applied to $V_{G2}$ for spin readout. **(c)** (Top) Schematic of the three stages pulse sequence applied to $V_{G2}$. (Bottom) Schematic energy diagrams at the different stages of the pulse sequence. $\mu_F$ is the chemical potential of the charge sensor playing the role of reservoir. A random spin is charged during the load stage. At the measure stage, if the loaded spin is up, the hole is able to tunnel out and is replaced by a spin down. On the opposite, if the loaded spin is down, tunneling in or out is impossible. Finally, the dot is discharged during the empty stage. **(d)** Phase versus time during the measurement stage. The orange curve exhibits a "blip" around $t = 50\,\mu$s, which indicates that the dot experienced a discharge/charge cycle characteristic of a spin up loading (see c). On the contrary, the red curve shows no phase change, which can be interpreted as a spin down loading. The phase signal is integrated over $6\,\mu$s.

As long as the dot and hole gases around remain sufficiently separated, the resulting $V_{\text{QD}}(\mathbf{r})$ is only weakly dependent on the choice of $\rho_{\text{test}}(\mathbf{r})$.

The wave functions in the potential $V_{\text{QD}}(\mathbf{r})$ are then calculated on the same mesh with a finite differences 6 bands $\mathbf{k}\cdot\mathbf{p}$ model[24]. We use Luttinger parameters $\gamma_1 = 4.285$, $\gamma_2 = 0.339$, $\gamma_3 = 1.446$, split-off energy $\Delta = 44$ meV and Zeeman parameter $\kappa = -0.42$. As discussed below, the first hole tends to localize in the two top corners of the channel overlapped by gate G2; However, given the width of the nanowire, an even weak disorder that breaks the symmetry between the left and right sides of the channel gives rise to two independent and non-degenerate "corner" dots (see discussion below)[23]. The $g$-tensor of the ground-state is finally computed along the lines of Ref.[24].

## B. Discussion

If the device was "planar", the hole would be confined at the top (001) facet of the channel by the quasi-vertical electric field of gate G2. It would, therefore, show the fingerprints of an almost pure (001) heavy-hole, with a large $g_x \simeq -6\kappa + 2\gamma_h \simeq 4.84$, and small $g_y$ and $g_z$ characteristic of the weak heavy-hole/light-hole mixing induced by the soft lateral confinement ($\gamma_h = 1.16$ being a correction that describes the heavy-hole/light-hole mixing by the magnetic vector potential)[26].

As the gate layout is actually non-planar, there is a also significant in-plane electric field component that drives the hole to

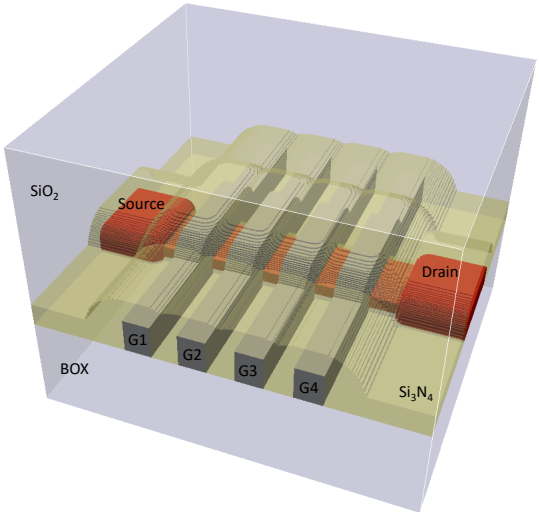


FIG. S.2. **Modeled structure.** The 17 nm thick and 100 nm wide silicon channel is connected to highly doped source and drain reservoirs and controlled by four gates G1...G4. The substrate below the BOX and the top gate above the structure (at the Metal 1 level) are grounded.

the lateral $\{1\bar{1}0\}$ facets. Given the width of the device, the hole is very responsive to that lateral electric field, and gets readily squeezed near one of the top corners of the channel, in a dot with comparable vertical and lateral extensions. This admixes a light-hole envelope into the hole wave function, which results in a decrease of $g_x$ ($\partial g_x/\partial V_{\rm G2} > 0$) and an increase of $g_y$ and $g_z$ ($\partial g_z/\partial V_{\rm G2} < 0$)[26,37]. This is evidenced in Fig. S.3, in a simpler setup with no hole gases under G1, G3 and G4. The mixing is particularly strong here because the structural vertical confinement is weak ($H = 17$ nm) so that the heavy-hole/light-hole gap is small. The $g$-factors (especially $g_x$ and $g_y$) tend to saturate rapidly with increasingly negative $V_{\rm G2}$ as the heavily squeezed hole responds less and less to the (vertical and lateral) electric fields ($|\partial g_x/\partial V_{\rm G2}| \ll |\partial g_z/\partial V_{\rm G2}|$).

Once screening by the holes gases is accounted for, the lateral electric field is however too weak to match the measured $g$-factors at the experimental bias point. This is highlighted in Fig. S.4, where the symbols are the experimental $g$-factors and the dashed lines are the calculated ones. $g_y$ remains actually smaller that $g_x$ (at $\theta_{zx} = \theta_{zy} = 90°$). This discrepancy may result from inaccuracies in the Thomas-Fermi screening, and (more likely) from disorder. In particular, holes in the channel may be captured by traps at the $Si/SiO_2$ interface ($P_b$ defects)[38], and holes in the poly-silicon gates by traps in the $Si_3N_4$ spacers. Such positively charged traps tend to strengthen confinement in the corners. We can achieve similar $g$-factors with different combinations of $P_b$ and bulk defects densities; the data displayed in the main text and in Fig. S.4 (solid lines) are computed with a density $\sigma_{\rm trap} = 5 \times 10^{10}$ $P_b$ defects/cm$^2$ at the $Si/SiO_2$ interface and a density $\rho_{\rm trap} = 5 \times 10^{17}$ traps/cm$^3$ in $Si_3N_4$. This $\sigma_{\rm trap}$ is typical of $Si/SiO_2$ interface, while the chosen $\rho_{\rm trap}$ does not seem unrealistic given the known affinity of nitrides for charges[39]. The model reproduces the main features of the experimental data – including the magnitude of the $g$-factors and the overall dependence of $f_L$ on $V_{\rm G1}$ and $V_{\rm G2}$ (Fig. 2 of the main text). Note that the action of $V_{\rm G1}$ is strongly screened by the hole gas beneath. In the absence of such screening and disorder, most electric field lines connect gate G2 to gates G1 and G3, so that the Larmor frequency of the hole is primarily a function of $V_{\rm G2} - (V_{\rm G1} + V_{\rm G3})/2$, and $\partial f_L/\partial V_{\rm G1} \approx -(\partial f_L/\partial V_{\rm G2})/2$ ($\rm LSES_{G1}$ and $\rm LSES_{G2}$ have nearby zeros).

The traps are introduced as a random distribution of point charges at the $Si/SiO_2$ interface and in $Si_3N_4$. This gives rise to variability in the $g$-factors and in their derivatives (dependence on the particular realization of the disorder[38]). This is outlined in Fig. S.5, which shows the $g$-factors calculated in 50 devices with different samples of disorder. For the sake of completeness, interface roughness is also included in Figs. S.4, S.5, and in Figs. 1 and 2 of the main text. It is characterized by rms fluctuations $\Delta = 0.3$ nm and correlation length $L_c = 8$ nm[38]. Fourty-four out of the 50 devices still show $g$-factors in reasonable agreement with the experiment. In the 3 devices featuring large $g_x$ and small $g_y$, the hole remains squeezed at the top interface by a $P_b$ defects near the corners. The variability is stronger for $\partial f_L/\partial V_{\rm G2}$, and especially for $\partial f_L/\partial V_{\rm G1}$. Although the agreement with theory is not perfect, the measured $\partial f_L/\partial V_{\rm G1} < 0$ whatever $\theta_{zx}$ suggests the presence of a charged $P_b$ defect in the vicinity of gate G2 that shifts the dot at least 10 nm towards gate G3. Alternatively, the dot might be shifted towards gate G3 by residual in-plane electric fields not accounted for accurately by the Thomas-Fermi approximation.

Choosing [001] as the quantization axis, the hole wave function is a strong mixture of heavy ($\approx 54\%\,|3/2, \pm 3/2\rangle_{[001]}$) and light ($\approx 43\%\,|3/2, \pm 1/2\rangle_{[001]}$) envelopes (the reminder being a split-off component). Choosing instead $y = [1\bar{1}0]$ as the quantization axis, the hole appears as a majority $\approx 85\%\,|3/2, \pm 3/2\rangle_{[1\bar{1}0]}$ envelope admixed with a minority $\approx 12\%\,|3/2, \pm 1/2\rangle_{[1\bar{1}0]}$ component. The measured and computed $g_y > g_x$ is the salient fingerprint of the prevalence of $|3/2, \pm 3/2\rangle_{[1\bar{1}0]}$ over $|3/2, \pm 3/2\rangle_{[001]}$ components. The confinement being comparable along $x$ and $y$, the hole actually appears purest when quantized along $z = [110]$, where it stands as a $\approx 90\%\,|3/2, \pm 1/2\rangle_{[1\bar{1}0]}$ envelope (as expected from $g_z < g_x, g_y$)[25].

We now discuss the remaining discrepancies with the experiment. The principal axes $X$, $Y$, $Z$ of the calculated $g$-tensor are almost perfectly aligned with the device $x$, $y$ and $z$ axes, whereas those of the experimental $g$-tensor are slightly rotated [by

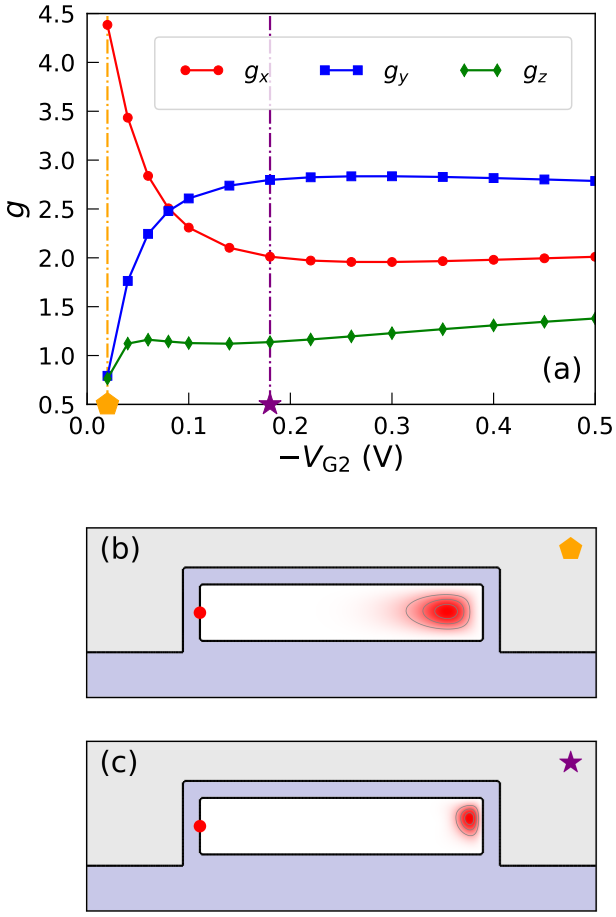


FIG. S.3. **Dependence of the $g$-factors on the electric field. (a)** $g$-factors $g_x$, $g_y$, and $g_z$ as a function of the difference of potential $-V_{G2}$ between gates G2 and gates G1 and G3 (both grounded). The larger $-V_{G2}$, the stronger the vertical and lateral electric fields. **(b, c)** Maps of the squared wave functions in the cross section of the channel below gate G2, at the biases marked with an orange pentagon and a purple star in (a). The channel is colored in white, the gate G2 in gray and $SiO_2$ in light blue. In these calculations, the density of traps $\rho_{\text{trap}}(\mathbf{r})$ is zero, except for a single positive charge on the left facet of the channel [red dot in (b, c)] introduced to lift the degeneracy between the left and right corner dots. The screening by the hole gases is also discarded (no hole accumulations anywhere).

$\approx 10^\circ$ around $x$ ($xyz \to xYz'$), then $\approx -25^\circ$ around $Y$ ($xYz' \to XYZ$)]. The calculated $g$-factors shown in Figs. 1 and 2 of the main text, and in Figs. S.4 and S.5 have been transformed accordingly as if these rotations resulted from a misalignment of the sample with respect to the magnet axes. However, the large rotation around $Y$ can hardly be accounted for by such a misalignment only. The fact that $Z$ is not aligned along the channel implies a loss of the $xy$ quasi-symmetry plane of gate G2[24], and the existence of additional heavy-hole/light-hole mixing mechanisms. The most likely scenario is that QD2 is slightly displaced towards G3 (as suggested above), and experiences small process and cool-down strains[24,30]. In particular, shear strains control the phase of the heavy-hole/light-hole mixing matrix elements. In the basis set and axes set of Ref.[26], they give rise to non-diagonal corrections to the $g$-matrix:

$$\delta g_{zy} \approx \frac{4\sqrt{3}\kappa d}{\Delta}\varepsilon_{yz},\ \delta g_{zx} \approx \frac{4\sqrt{3}\kappa d}{\Delta}\varepsilon_{xz},\ \delta g_{xy} = -\delta g_{yx} \approx -\frac{12\kappa b}{\Delta}\varepsilon_{xy}\,, \tag{5}$$

where $b = -2.1$ eV and $d = -4.85$ eV are the uniaxial and shear deformation potentials of the valence band of silicon, and $\Delta$ is the heavy-hole/light-hole gap. Therefore, the shear strains $\varepsilon_{yz}$, $\varepsilon_{xz}$, and $\varepsilon_{xy}$ drive rotations of the principal magnetic axes around $x$, $y$ and $z$ respectively. We can recover the experimental rotations assuming small $\varepsilon_{yz} \simeq 0.035\%$ and $\varepsilon_{xz} \simeq 0.080\%$, which highlights the sensitivity of such quantum devices to residual strains[24,30,40]. Note that the possible rotation of the principal axes around $z$ can not be resolved since the $g$-factors have not been measured in the $xy$ plane (but may improve the overall agreement between theory and experiment, in particular for $\text{LSES}_{\text{G1}}$); The detailed assessment of strains in such complex

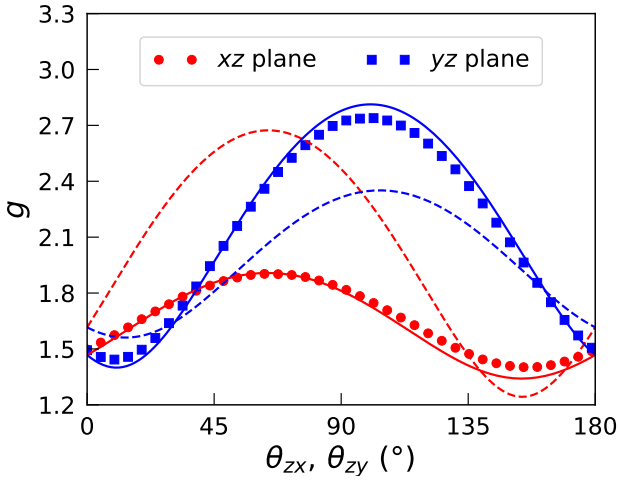


FIG. S.4. **Comparison between the experimental and calculated $g$-factors.** The $g$-factors are plotted in the $xz$ (red) and $yz$ (blue) planes, as a function of the angles $\theta_{zx}$ and $\theta_{zy}$, respectively. The symbols are the experimental data; the dotted lines the data calculated in the pristine device; and the solid lines the data calculated in a device with interface roughness and charged traps at the $Si/SiO_2$ interface and in $Si_3N_4$ (see text). These traps tend to strengthen confinement on the lateral facet.

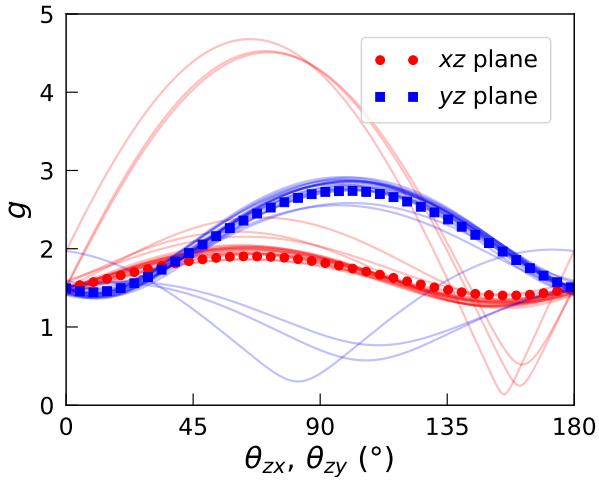


FIG. S.5. **Variability of the calculated $g$-factors.** Same as Fig. S.4; Each line is a different realization of the interface roughness and charge disorder. The interface roughness rms is $\Delta = 0.3$ nm and the correlation length is $L_c = 8$ nm[38]; The density of positively charged traps is $\sigma_{\rm trap} = 5 \times 10^{10}$ cm$^{-2}$ at the $Si/SiO_2$ interface, and $\rho_{\rm trap} = 5 \times 10^{17}$ cm$^{-3}$ in $Si_3N_4$.

nanostructures is, however, difficult (in particular in the nitrides), and goes beyond the scope of this work. Since uniaxial and shear strains rule the heavy-hole/light-hole mixing together with confinement, they can in principle help reduce the lateral confinement, hence the disorder needed to reach agreement with the experimental $g$-factors. We emphasize, though, that the dot becomes much more responsive to G2 once deconfined from the corner, so that $\partial f_L/\partial V_{\rm G2}$ increases significantly. Therefore, the magnitude of the experimental $\partial f_L/\partial V_{\rm G2}$, as well as the fact that the experimental $g$-factors match the saturation values calculated at large gate voltage (Fig. S.3), support pretty strong confinement in the corner and small strains.

To conclude, the present model captures and explains the most salient features of the experiment: the anisotropy of the $g$-factors, $g_y > g_x > g_z$, and of $\partial f_L/\partial V_{\rm G2}$ result from the balance between vertical and lateral confinement in the corner dot of a "thick" silicon film; $\partial f_L/\partial V_{\rm G1}$ is strongly screened by the hole gas accumulated under gate G1 and is, therefore, much smaller (in magnitude) than $\partial f_L/\partial V_{\rm G2}$. The remaining discrepancies (in particular the rotation of the principal axes of the $g$-tensor) are attributed to residual process and cool-down strains and to possible inaccuracies in the description of screening.

Since $g_x$ saturates faster than $g_z$ with increasing electric field (Fig. S.3), the magnetic field orientations $\theta_{zx}$ at which $\partial f_L/\partial V_{\rm G2} = 0$ depend on the strength of the electric field, and in particular on the ratio between the lateral and vertical components. This ratio can be controlled in an alternative "face-to-face" layout where G2 is split in two independent gates

$G_{2L}$ and $G_{2R}$ that overlap the left (L) and right (R) corners respectively[41]. $G_{2R}$ can then be used to strengthen the lateral electric field in the left dot. This opens interesting opportunities for the exploration of the manipulation, lifetimes and physics of hole spins.

## S3. LSES WITH RESPECT TO GATE 2 ($\mathrm{LSES_{G2}}$)

To measure $\mathrm{LSES_{G2}}$, we apply a two stage sequence (Initialisation/Measure and Control) on MW2 while bursting for 5 $\mu$s on MW1 to drive coherent spin rotations (see Fig. S.6a). We record the oscillations of $P_\uparrow$ (averaged over 200 pulse sequences) as a function of the MW1 burst frequency $f_{\mathrm{MW1}}$ (Fig. S.6b), and fit with a Rabi chevron model to extract the Larmor frequency $f_L$.

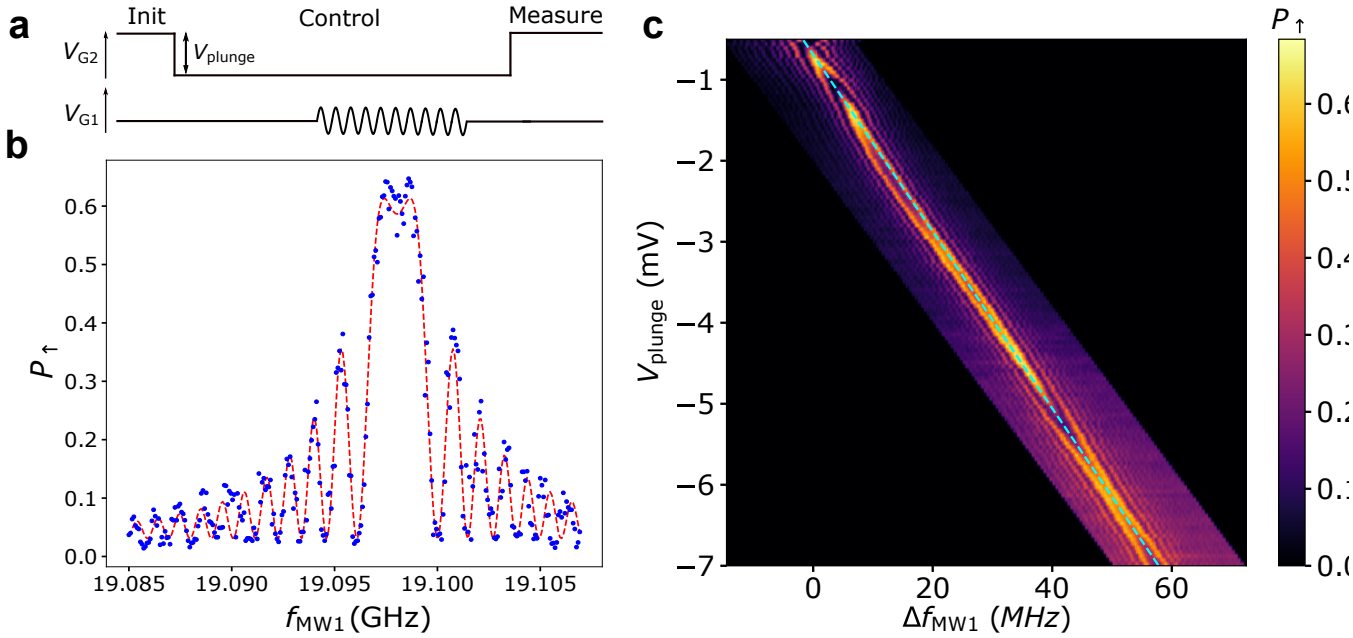


FIG. S.6. **Measurement of $\mathrm{LSES_{G2}}$. (a)** Schematic representation of the pulse sequence used to monitor spin resonance. We burst on MW1 for 5 $\mu$s and average $P_\uparrow$ over 200 such sequences. **(b)** Average $P_\uparrow$ (Blue dots) versus MW1 burst frequency at $V_{\mathrm{plunge}} = -1$ mV. This plot is in essence a line cut of a Rabi chevron at $t_{\mathrm{burst}} = 5\,\mu$s. The red dashed line is a fit used to extract the Larmor frequency. **(c)** Tracking of $f_L$ as a function of $V_{\mathrm{plunge}}$. The dashed blue line is a linear fit whose slope is equal to $\mathrm{LSES_{G2}}$.

We repeat the experiment for different $V_{\mathrm{plunge}}$, and obtain the map of Fig. S.6c, where $\mathrm{LSES_{G2}} = \partial f_L / \partial V_{\mathrm{plunge}}$ is the slope of the dashed blue line. Note that the Rabi frequency also depends on $V_{\mathrm{plunge}}$.

## S4. RABI OSCILLATIONS AT THE SWEET SPOT

Sweet spots for coherence may result from a simple zero of the longitudinal spin-electric susceptibility, or from the complete decoupling of the hole from the electric field (for example if the wave function becomes centrosymmetric[24]). In the latter case, Rabi oscillations (transverse spin-electric susceptibility) are also impossible. Figure S.7 demonstrates that the hole can still be manipulated electrically near the sweet spot for coherence at $\theta_{zx} = 99°$. In the experiment reported in the main text, the hole is driven by a microwave burst on gate G1. The Rabi frequency is found dependent on the magnetic field orientation (data not shown here), with a minimum around the sweet spot, where the hole spin still rotates up to $F_{\mathrm{Rabi}} = 5$ MHz for an applied power of 20 dBm on top of the MW1 line. A microwave burst on gate G2 also enables spin rotation up to $\sim 3$ MHz at the sweet spot (see Fig. S.7d). However, we speculate that the Rabi frequency is only limited by the available microwave power and the line attenuation, since we do not observe any saturation with increasing power. After conversion of the microwave power into gate voltage amplitudes, we find that the driving efficiency is much larger on gate G2 ($F_{\mathrm{Rabi}} = 7.6$ MHz/mV) than on gate G1 ($F_{\mathrm{Rabi}} = 1.2$ MHz/mV), which suggests that the spin could be rotated much faster by reducing the attenuation on the MW2 line.

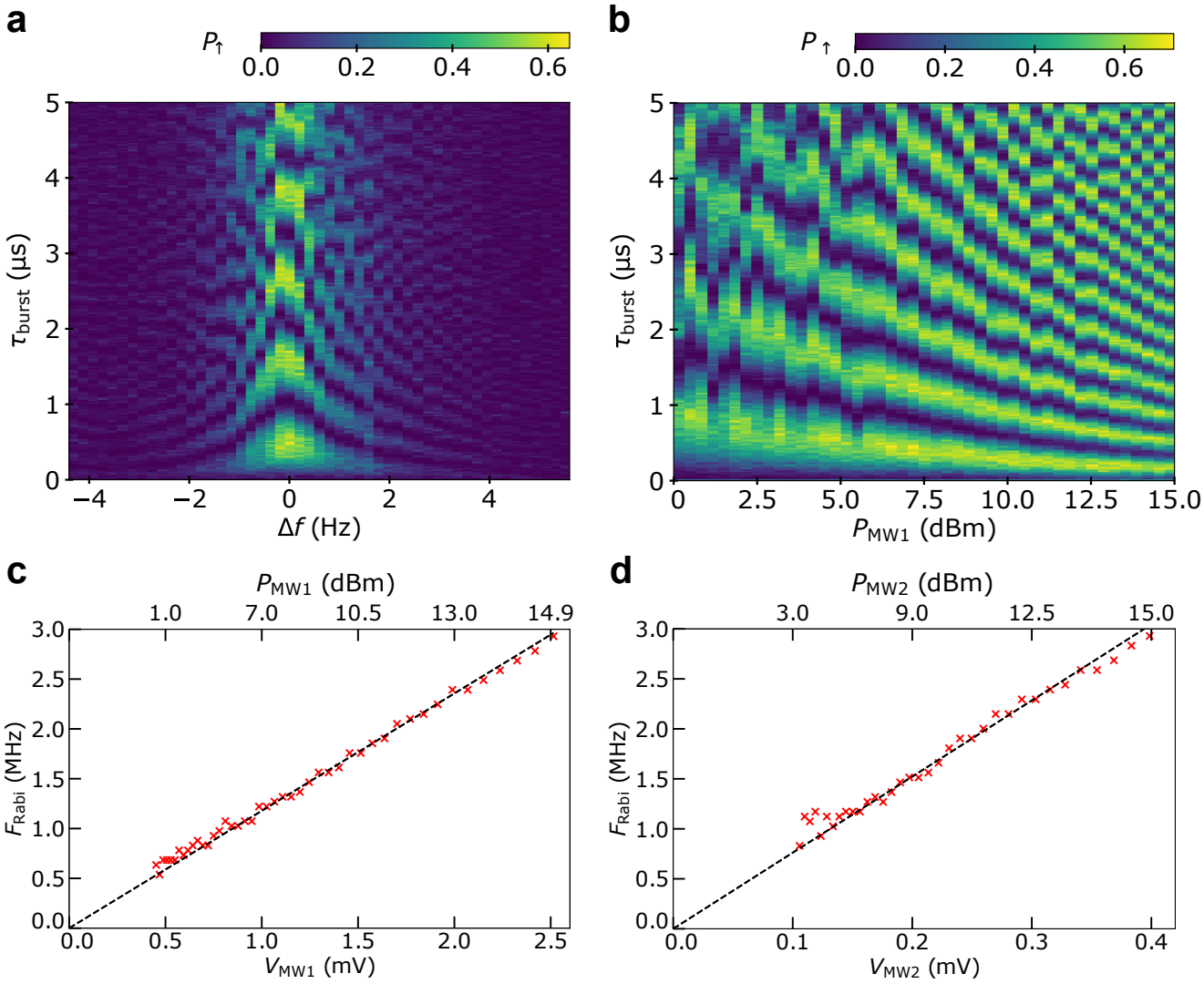


FIG. S.7. **Electrical spin driving at the coherence sweet spot (a)** Chevron pattern at $\theta_{zx} = 99°$ recorded with the same pulse sequence as in Fig. S.6a. $P_\uparrow$ is plotted versus MW1 detuning from spin resonance ($\Delta f = f_{\mathrm{MW1}} - f_L$) and MW1 burst duration $\tau_{\mathrm{burst}}$. The Larmor frequency is $f_L = 17\,\mathrm{GHz}$ and the MW1 power on top of the fridge is $P_{\mathrm{MW1}} = 5\,\mathrm{dBm}$. **(b)** $P_\uparrow$ versus $P_{\mathrm{MW1}}$ and $\tau_{\mathrm{burst}}$ for $\Delta f = 0$. **(c)** Rabi frequency extracted from (b) versus MW1 amplitude on chip (symbols) assuming 30 dB attenuation from attenuators and 30 dB loss from cables at low temperature. The top axis is the power delivered on top of the fridge. The dashed line is a linear fit with slope $F_{\mathrm{Rabi}} = 1.2\,\mathrm{MHz/mV}$, which evidences the absence of saturation at least up to 3 MHz. **(d)** Same as (c) but driving the spin using G2. The attenuation is larger on this line (46 dBm), so that the Rabi oscillations are actually 6 times faster on G2 (slope $F_{\mathrm{Rabi}} = 7.6\,\mathrm{MHz/mV}$) than on G1.

## S5. PURE DEPHASING WITH UNCORRELATED NOISE SOURCES

The hole can generally be described as an effective spin 1/2 with Hamiltonian[28]

$$H_s = \mathbf{S} \cdot \boldsymbol{\omega}_L(\mathbf{V}_{\mathrm{G}})\,. \tag{6}$$

Here $\mathbf{S} = \frac{\hbar}{2}\boldsymbol{\sigma}$ is the spin 1/2 operator and $\boldsymbol{\omega}_L(\mathbf{V}_{\mathrm{G}}) = \frac{\mu_B}{\hbar}\,\mathrm{g}(\mathbf{V}_{\mathrm{G}}) \cdot \mathbf{B}$ stands for the spin precession (Larmor) vector, proportional to the product of the voltage-dependent $g$-tensor (or $g$-matrix[42]) $\mathrm{g}(\mathbf{V}_{\mathrm{G}})$ with the external magnetic field $\mathbf{B}$. $\mathbf{V}_{\mathrm{G}} = (V_{\mathrm{G1}}, V_{\mathrm{G2}}, \ldots, V_{\mathrm{G}n})$ is the set of voltages on gates G1, G2, …, G$n$. Each can be split into static and dynamical contributions $V_{\mathrm{G}i}(t) = V^0_{\mathrm{G}i} + \delta V_{\mathrm{G}i}(t)$, $\mathrm{V}^0_{\mathrm{G}i}$ being the bias voltage on gate G$i$ and $\delta V_{\mathrm{G}i}(t)$ the voltage noise responsible for qubit relaxation and decoherence.

The gate voltage noise introduces a random component $\delta\phi(t)$ to the qubit phase $\phi(t) = 2\pi f_L t + \delta\phi(t)$, where $f_L = \frac{\mu_B}{h}|\,\mathrm{g}(\mathbf{V}^0_{\mathrm{G}})\cdot$

$\mathbf{B}|$ is the Larmor frequency. After free evolution over time $t$ the accumulated random phase reads at first order in the noise[43,44]:

$$\delta\phi(t) = 2\pi \int_0^t dt'\, \delta f_L(t') = 2\pi \int_0^t dt' \sum_i D_{\mathrm{G}i}\delta V_{\mathrm{G}i}(t')\,. \tag{7}$$

where $D_{\mathrm{G}i} = \partial f_L/\partial V^0_{\mathrm{G}i}$ is the LSES of gate G$i$. More generally, for a dynamical decoupling pulse sequence the accumulated phase is:[43–47]

$$\delta\phi(t) = 2\pi \int_{-\infty}^{+\infty} dt' \sum_i D_{\mathrm{G}i}\delta V_{\mathrm{G}i}(t')\,\eta_t(t')\,, \tag{8}$$

where the function $\eta_t(t')$ describes the effects of the pulse sequence performed over time $t$. In particular, for free induction decay (Ramsey experiment),

$$\eta_t{}^{\mathrm{R}}(t') = \begin{cases} 1 & \text{if } 0 < t' < t, \\ 0 & \text{otherwise}\,, \end{cases} \tag{9}$$

and for a CPMG sequence with $N_\pi$ $\pi$-pulses[48]:

$$\eta_t{}^{\mathrm{CPMG}}(t') = \sum_{k=0}^{N_\pi} (-1)^k \theta(t_{k+1} - t')\theta(t' - t_k)\,, \tag{10}$$

where $\theta$ is the Heaviside function, $t_k = (k-1/2)t/N_\pi$ for $k = 1, \ldots, N_\pi$, and by definition[48] $t_0 = 0$ and $t_{N_\pi+1} = t$. The Ramsey and the Hahn echo experiments are particular cases of the CPMG sequence with $N_\pi = 0$ and $N_\pi = 1$ respectively.

The dephasing experienced by the spin as a consequence of voltage noise is characterized by the decay of the off-diagonal element of the spin density matrix in the rotating frame[44]:

$$\langle\tilde{\rho}_{01}\rangle(t) = \tilde{\rho}_{01}(0)\langle e^{i\delta\phi(t)}\rangle = \tilde{\rho}_{01}(0)e^{-\frac{1}{2}\langle\delta\phi^2(t)\rangle}\,, \tag{11}$$

where $\langle\cdot\rangle$ denotes an ensemble average (over the random processes), and, for the general pulse sequence:

$$\langle\delta\phi^2(t)\rangle = 4\pi^2 \int_{-\infty}^{+\infty} dt' \int_{-\infty}^{+\infty} dt'' \sum_{i,j} D_{\mathrm{G}i}D_{\mathrm{G}_j}\langle\delta V_{\mathrm{G}i}(t')\delta V_{\mathrm{G}j}(t'')\rangle\,\eta_t(t')\,\eta_t(t'')\,. \tag{12}$$

Under the assumptions that the noise on the different gates are independent, and that their respective auto-correlation functions are homogeneous in time, we reach in frequency domain:

$$\langle\delta\phi^2(t)\rangle = 4\pi^2 \int_{-\infty}^{+\infty} df \sum_i D^2_{\mathrm{G}i}S_{\mathrm{G}i}(f)\,|\tilde{\eta}_t(f)|^2\,, \tag{13}$$

where $S_{\mathrm{G}n}(f) = \int_{-\infty}^{+\infty} dt\, e^{-2i\pi ft}\,\langle\delta V_{\mathrm{G}n}(t)\delta V_{\mathrm{G}n}(0)\rangle$ is the Fourier transform of the auto-correlation function of the noise on gate G$n$ (the power spectrum according to the Wiener-Khinchin theorem), and $\tilde{\eta}_t(f) = \int_{-\infty}^{+\infty} dt\, e^{-2i\pi ft}\,\eta_t(t)$. Eq. (13) can also be formalized using the filter function concept[44,48,49]. We analyze below the different pulse sequences relevant for the present experiments.

### A. Free induction decay

For the Ramsey sequence we have

$$\left|\tilde{\eta}_t{}^{\mathrm{R}}(f)\right|^2 = \left(\frac{\sin(\pi ft)}{\pi f}\right)^2\,. \tag{14}$$

Therefore, $\left|\tilde{\eta}_t{}^{\mathrm{R}}(f)\right|^2/t^2$ is close to unity up to $|f| \sim 1/t \sim 1/T_2^*$, so that free induction decay is sensitive to noise in this whole range of frequencies. For low-frequency noise spectra of the form $S_{\mathrm{G}i}(f) = S^{\mathrm{lf}}_{\mathrm{G}i}\, f_0/\max(|f|, f_l)$ together with a (soft) high-frequency cutoff $f_h$, we get in the regime $2\pi f_l \ll 2\pi f_h \ll 1/t$:

$$\exp\left(-\frac{1}{2}\langle\delta\phi_R(t)^2\rangle\right) \approx \exp\left[-4\pi^2 t^2 \ln\left(\frac{f_h}{f_l}\right) f_0 \sum_i D^2_{\mathrm{G}i}\, S^{\mathrm{lf}}_{\mathrm{G}i}\right] \equiv \exp\left[-\left(\frac{t}{T_2^*}\right)^2\right]\,, \tag{15}$$

with[43]:

$$\frac{1}{T_2^*} \approx 2\pi\sqrt{\ln\left(\frac{f_h}{f_l}\right) f_0 \sum_i D^2_{\mathrm{G}i}\, S^{\mathrm{lf}}_{\mathrm{G}i}}\,. \tag{16}$$

As shown in the main text (Fig. 4), the averaged $T_2^*$ decreases with increasing $t_{\mathrm{meas}} \sim 1/(2\pi f_l)$ as the experiment probes smaller and smaller noise frequencies.

We can also estimate the contribution of higher frequency noises with spectra $S_{\mathrm{G}i}(f) = S_{\mathrm{G}i}^{\mathrm{hf}}\sqrt{f_0/f}$. The Ramsey oscillations then decay as $\exp(-\frac{1}{2}\langle\delta\phi_R(t)^2\rangle) = \exp(-(t/T_{2,\mathrm{hf}}^*)^{3/2})$, where we define:

$$\frac{1}{T_{2,\mathrm{hf}}^*} = \left(\frac{16\pi^2}{3} f_0^{1/2} \sum_i D_{\mathrm{G}i}^2 S_{\mathrm{G}i}^{\mathrm{hf}}\right)^{2/3} \approx 14 \left(f_0^{1/2} \sum_i D_{\mathrm{G}i}^2 S_{\mathrm{G}i}^{\mathrm{hf}}\right)^{2/3} . \tag{17}$$

The low-frequency and high-frequency contributions to the decay of the Ramsey signal cross over at time $t_* = T_2^*(T_2^*/T_{2,\mathrm{hf}}^*)^3 \ll T_2^*$ when $T_2^* \ll T_{2,\mathrm{hf}}^*$, and the decay is dominated by the low-frequency noise when $t \gg t_*$.

### B. Hahn Echo sequence

For the Hahn echo sequence,

$$\left|\tilde{\eta}_t{}^{\mathrm{E}}(f)\right|^2 = \frac{\sin^4(\pi f t/2)}{(\pi f/2)^2} . \tag{18}$$

Therefore, the integrand in Eq. (13) is small at frequencies $|f| \ll 1/t$ and the integral is dominated by the region around $f_* = 2/(\pi t)$ (with extent $\sim f_*$). $f_*$ is of the order of $10 - 100\,\mathrm{kHz}$ for Hahn-echo sequences with total length $t = 10 - 100\,\mu\mathrm{s}$. If in this range of frequencies the noise spectra are of the form $S_{\mathrm{G}i}(f) = S_{\mathrm{G}i}^{\mathrm{hf}}(f_0/f)^\alpha$ ($0 < \alpha \leq 2$ typically), then:

$$\exp\left(-\frac{1}{2}\langle\delta\phi_E(t)^2\rangle\right) = \exp\left(-C_\alpha(2\pi t)^{\alpha+1} f_0^\alpha \sum_i D_{\mathrm{G}i}^2 S_{\mathrm{G}i}^{\mathrm{hf}}\right) \equiv \exp\left[-\left(\frac{t}{T_2^{\mathrm{E}}}\right)^{\alpha+1}\right] , \tag{19}$$

where $C_\alpha = 2\sin(\frac{\alpha\pi}{2})(2^{1-\alpha} - 1)\Gamma(-1-\alpha)$, with $\Gamma$ the Gamma function[50], and:

$$\frac{1}{T_2^{\mathrm{E}}} = 2\pi \left(C_\alpha f_0^\alpha \sum_i D_{\mathrm{G}i}^2 S_{\mathrm{G}i}^{\mathrm{hf}}\right)^{\frac{1}{\alpha+1}} . \tag{20}$$

In the particular case $\alpha = 0.5$ (see main text), $C_{0.5} = \frac{4\sqrt{2\pi}}{3}(2^{1/2} - 1) \approx 1.38$, so that:

$$\frac{1}{T_2^{\mathrm{E}}} \approx 7.8 \left(f_0^{1/2} \sum_i D_{\mathrm{G}i}^2 S_{\mathrm{G}i}^{\mathrm{hf}}\right)^{2/3} . \tag{21}$$

The Hahn echo $T_2^{\mathrm{E}}$ and Ramsey $T_{2,\mathrm{hf}}^*$ [Eq. (17)] are thus proportional. Therefore, one would expect $T_{2,\mathrm{hf}}^* \simeq 50\,\mu\mathrm{s}$ at $\theta_{zx} = 99^\circ$ where $T_2^{\mathrm{E}} \simeq 90\,\mu\mathrm{s}$ if the limiting noise mechanisms were the same at low and high frequency. The much shorter $T_2^*$ measured in the present device hence support the existence of additional noise sources at low frequency.

### C. CPMG sequence

For the more general CPMG sequence[48,51] with noise spectra $S_{\mathrm{G}i}^{\mathrm{hf}}(f_0/f)^\alpha$ over extent $\sim 1/t$ around the frequency $f_{N_\pi} = N_\pi/(2t) \sim N_\pi/(2T_2^{\mathrm{CPMG}})$, we get the scaling

$$\langle\delta\phi^2(t)\rangle \sim t^{\alpha+1} N_\pi^{-\alpha} f_0^\alpha \sum_i D_{\mathrm{G}i}^2 S_{\mathrm{G}i}^{\mathrm{hf}} , \tag{22}$$

so that $\langle\delta\phi^2(t)\rangle \sim (t/T_2^{\mathrm{CPMG}})^{\alpha+1}$, with:

$$T_2^{\mathrm{CPMG}} \sim N_\pi^\gamma f_0^{-\gamma} \left(\sum_i D_{\mathrm{G}i}^2 S_{\mathrm{G}i}^{\mathrm{hf}}\right)^{-\frac{1}{\alpha+1}} \tag{23}$$

and $\gamma = \alpha/(\alpha+1)$, in agreement with Ref. 51.

## S6. NOISE SPECTRUM

We measured 3700 Ramsey fringes over $t_{\mathrm{tot}} = 10.26$ hours. For each realization, we varied the free evolution time $\tau_{\mathrm{wait}}$ up to $7\,\mu\mathrm{s}$, and averaged 200 single shot spin measurement to obtain $P_\uparrow$ (see Fig. S.8a (top)). The fringes oscillate at the detuning $\Delta f = |f_{\mathrm{MW1}} - f_L|$ between the MW1 frequency $f_{\mathrm{MW1}}$ and the spin resonance frequency $f_L$. In order to track low frequency noise on $f_L$, we make a Fourier transform of each fringe and extract its fundamental frequency $\Delta f$ reported in Fig. S.8a (bottom). During the whole experiment, $f_{\mathrm{MW1}}$ is set to 17 GHz.

The low frequency spectral noise on the Larmor frequency (in units of $\mathrm{Hz}^2/\mathrm{Hz}$) is calculated[52] from $\Delta f(t)$ as[4]:

$$S_L = \frac{t_{\mathrm{tot}} \left|\mathrm{FFT}[\Delta f]\right|^2}{N^2}\,, \tag{24}$$

where $\mathrm{FFT}[\Delta f]$ is the fast Fourier transform (FFT) of $\Delta f(t)$ and $N$ is the number of sampling points. We observe that the low frequency noise, plotted in Fig. S.8b, behaves approximately as $S_L(f) = S^{\mathrm{lf}}(f_0/f)$ with $S^{\mathrm{lf}} = 10^9\,\mathrm{Hz}^2/\mathrm{Hz}$, which is comparable to what has been measured for a hole spin in natural Germanium[53].

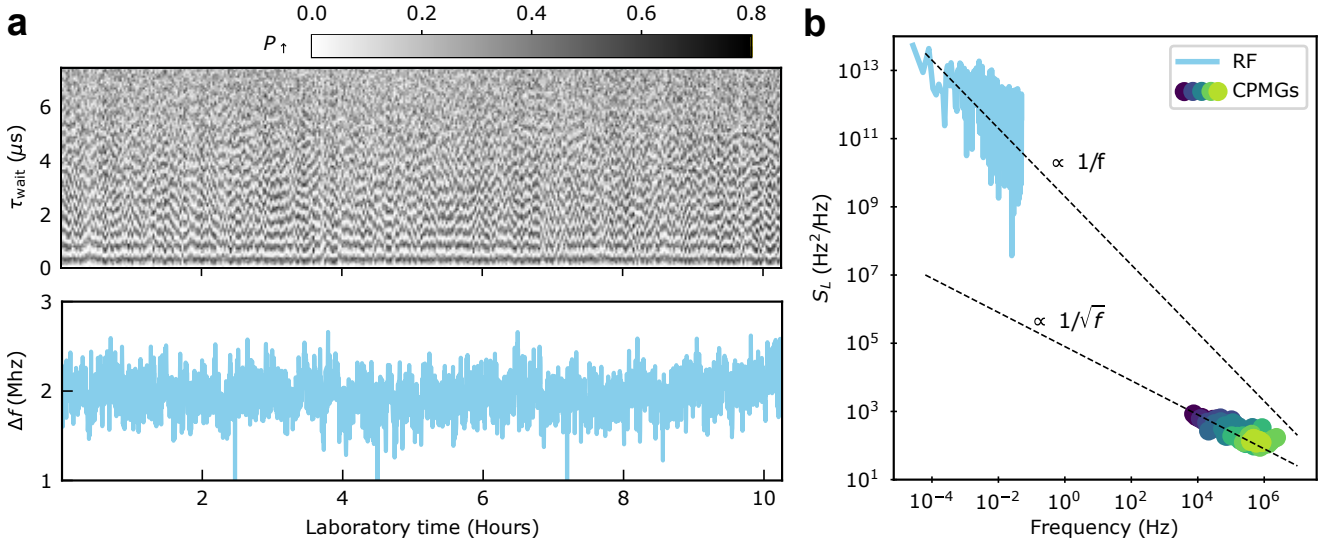


FIG. S.8. **Noise spectrum (a)** (top) Ramsey fringes as a function of $\tau_{\mathrm{wait}}$ acquired during 10 hours, at $\theta_{zx} = 90°$. Each fringe oscillates at the frequency $\Delta f = f_{\mathrm{MW1}} - f_{\mathrm{L}}$. A single fringe takes roughly 10 s to record. (bottom) $\Delta f$, obtained via Fourier transform of the Ramsey fringes, versus laboratory time. **(b)** Power spectral density of the noise on the Larmor frequency. The low frequency spectrum (RF) is calculated from (a) and is roughly proportional to $1/f$, as outlined by the upper dashed line. The high frequency spectrum (colored dots) is extracted from CPMG measurements with $N_\pi$ from 2 to 256, and is proportional to $1/f^{0.5}$ (lower dashed line).

To further characterize the noise spectrum, we add the CPMG measurements as colored dots on Fig. S.8b[4]:

$$S_L\left(N_\pi/(2\tau_{\mathrm{wait}})\right) = -\frac{\ln(A_{\mathrm{CPMG}})}{2\pi^2\tau_{\mathrm{wait}}}\,, \tag{25}$$

where $A_{\mathrm{CPMG}}$ is the normalized CPMG amplitude. As discussed in the main text, the resulting high frequency noise scales as $S^{\mathrm{hf}}(f_0/f)^{0.5}$, where $S^{\mathrm{hf}} = 8\times10^4\,\mathrm{Hz}^2/\mathrm{Hz}$ is four orders of magnitude lower than $S^{\mathrm{lf}}$. This high frequency noise appears to be dominated by electrical fluctuations (as supported by the correlations between the Hahn-echo/CPMG $T_2$ and the LSESs), whereas additional quasi-static contributions, including hyperfine interactions (see section S7), prevail at low frequency.

## S7. HYPERFINE INTERACTION LIMIT FOR THE INHOMOGENEOUS DEPHASING TIME

The hyperfine interactions between the hole and the $N$ nuclei spins are described by the following Hamiltonian[54,55]:

$$H_{\mathrm{int}} = \frac{A}{2n_0}\sum_{n=1}^{N}\delta(\mathbf{r}-\mathbf{R}_n)\otimes\mathbf{J}\cdot\mathbf{I}_n\,, \tag{26}$$

where $A$ is the hyperfine coupling constant, $n_0$ is the density of nuclei in the crystal, $\mathbf{I}_n$ is the spin operator of nuclei $n$ at position $\mathbf{R}_n$, and $\mathbf{J}$ is the angular momentum operator acting on the $J = 3/2$ Bloch functions of the heavy and light holes (whereas the $\delta(\mathbf{r}-\mathbf{R}_n)$ acts on the envelopes). We discard here the small contributions from the split-off $J = 1/2$ components as well as the small $\propto J_x^3$, $J_y^3$, $J_z^3$ corrections arising from the cubic symmetry of the crystal[54].

Let $|\uparrow\rangle$ and $|\downarrow\rangle$ be the pseudo-spin states of the dot at a given magnetic field, and $|\psi_{\mathrm{nucl}}\rangle$ be the nuclear configuration. The first-order correction to the Larmor energy $\varepsilon_L = hf_L$ is:

$$\delta\varepsilon_L = \frac{A}{2n_0}\sum_{n=1}^{N}\langle\psi_{\mathrm{nucl}}|\,\mathbf{I}_n\,|\psi_{\mathrm{nucl}}\rangle\cdot\left(\langle\uparrow|\,\delta(\mathbf{r}-\mathbf{R}_n)\otimes\mathbf{J}\,|\uparrow\rangle - \langle\downarrow|\,\delta(\mathbf{r}-\mathbf{R}_n)\otimes\mathbf{J}\,|\downarrow\rangle\right). \tag{27}$$

We next average over the nuclei configurations assuming uncorrelated and unpolarized nuclear spins with Gaussian-distributed quasi-static fluctuations[56]. The variance of $\delta\varepsilon_L$ is then:

$$\left\langle \delta\varepsilon_L^2 \right\rangle = \frac{A^2}{4n_0^2} \sum_{n=1}^{N} \left\langle I_x^2 \right\rangle \delta J_x^2(\mathbf{R}_n) + \left\langle I_y^2 \right\rangle \delta J_y^2(\mathbf{R}_n) + \left\langle I_z^2 \right\rangle \delta J_z^2(\mathbf{R}_n) \,, \tag{28}$$

where, for $\alpha \in \{x, y, z\}$:

$$\delta J_\alpha(\mathbf{R}_n) = \langle\uparrow| \, \delta(\mathbf{r} - \mathbf{R}_n) \otimes J_\alpha \, |\uparrow\rangle - \langle\downarrow| \, \delta(\mathbf{r} - \mathbf{R}_n) \otimes J_\alpha \, |\downarrow\rangle \,, \tag{29}$$

and $\left\langle I_x^2 \right\rangle = \left\langle I_y^2 \right\rangle = \left\langle I_z^2 \right\rangle = I(I+1)/3$. Taking a second average over nuclei spin distributions, and assuming slowly varying envelope functions, we reach:

$$\left\langle \left\langle \delta\varepsilon_L^2 \right\rangle \right\rangle = \frac{A^2}{12n_0} I(I+1)\nu \left( \overline{\delta J_x^2} + \overline{\delta J_y^2} + \overline{\delta J_z^2} \right) \,, \tag{30}$$

where $\nu$ is the fraction of nuclei carrying a spin, and:

$$\overline{\delta J_\alpha^2} = \int d^3\mathbf{R} \, \delta J_\alpha^2 \left( \mathbf{R} \right) \,. \tag{31}$$

Finally, the rate of inhomogeneous dephasing due to hyperfine interactions is[57,58]:

$$\Gamma_2^* = \frac{1}{T_2^*} = \frac{\sqrt{\left\langle \left\langle \delta\varepsilon_L^2 \right\rangle \right\rangle}}{\sqrt{2}\hbar} = \frac{|A|}{2\hbar} \sqrt{\frac{\nu I(I+1)}{6n_0}} \left( \overline{\delta J_x^2} + \overline{\delta J_y^2} + \overline{\delta J_z^2} \right)^{1/2} \,. \tag{32}$$

The above expression can be evaluated with the 6 bands $\mathbf{k} \cdot \mathbf{p}$ wave functions computed in section S2. For silicon, we use $n_0 = 49.94$ nm$^{-3}$, as well as $\nu = 4.7\%$, $I = 1/2$, and $|A| = 1.67\,\mu$eV for $^{29}$Si isotopes[55]. This value of $|A|$ was specifically computed for holes with *ab initio* density functional theory[59]. The resulting $T_2^*$, plotted as a dashed line in Fig. 4 of the main text, is minimal when the magnetic field $\mathbf{B}$ is along $y$, and maximal when it is in the $xz$ plane, as expected for a carrier that shows the strongest heavy-hole character when $\mathbf{J}$ is quantized along $y$. $T_2^*$ is weakly dependent on the angle $\theta_{zx}$, and is around $2.4\,\mu$s in the $xz$ plane.

## S8. SETUP

We operate in a dilution refrigerator system equipped with a three-axis vector superconducting magnet. However, one of the axis was broken during the experiment. Therefore, after recording Fig. 1d of the main text, the sample was warmed up, physically rotated by 90°, and cooled down again to record Fig. 1e. The main solenoid magnet produces a magnetic field of up to 6 T in the $z$ direction, while both transverse Helmholtz coils ramp up to 1 T in the $x$ and $y$ directions. The electrical lines connecting the sample are displayed in Fig. S.9. 24 twisted pairs are filtered at the mixing chamber by 6 low pass filters. The DC gate voltages are generated by Itest high stability voltage sources (BE2141). To perform charge and spin manipulation, semi-rigid coaxial lines with 20 GHz bandwidth are routed to G1, G2 and G3 using on-PCB bias tees. Microwave frequency signals are supplied by a vector signal generator (R&S SMW200A) with IQ modulating signals originating from two channels of an arbitrary waveform generator (AWG) Tektronix AWG5200. Other channels of the AWG are used to generate the pulse sequences. The homodyne readout of the resonator connected to the drain electrode is performed with a Zurich Instrument UHFLI lock-in with an excitation power of −105 dBm at the PCB stage. The reflected signal from the resonator is amplified at 4 K with an ultra-low noise cryogenic amplifier LNF-LNC0.2-3A.

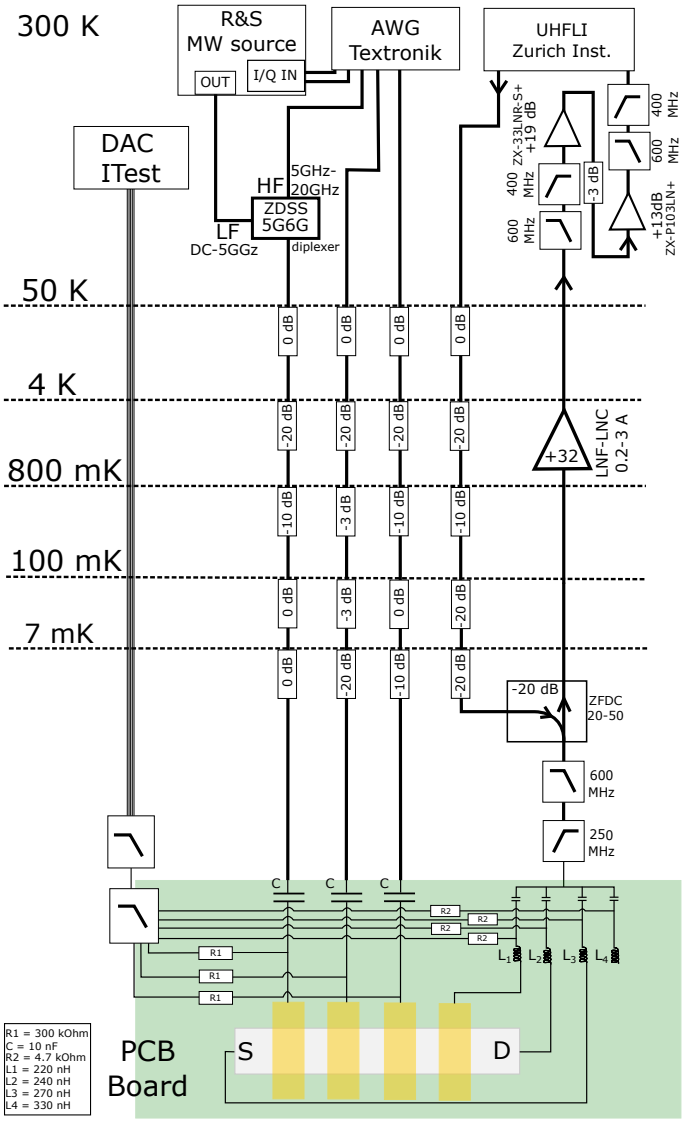


FIG. S.9. **Experimental setup.** Dilution fridge with all electrical connections to the sample.


[1] D. Loss and D. P. DiVincenzo, *"Quantum computation with quantum dots,"* Physical Review A **57**, 120 (1998).

[2] G. Burkard, T. D. Ladd, J. M. Nichol, A. Pan, and J. R. Petta, "Semiconductor spin qubits," (2021), arXiv:2112.08863 [cond-mat.mes-hall].

[3] M. Veldhorst, J. C. C. Hwang, C. H. Yang, A. W. Leenstra, B. de Ronde, J. P. Dehollain, J. T. Muhonen, F. E. Hudson, K. M. Itoh, A. Morello, and A. S. Dzurak, *"An addressable quantum dot qubit with fault-tolerant control-fidelity,"* Nature Nanotechnology **9**, 981 (2014).

[4] J. Yoneda, K. Takeda, T. Otsuka, T. Nakajima, M. R. Delbecq, G. Allison, T. Honda, T. Kodera, S. Oda, Y. Hoshi, N. Usami, K. M. Itoh, and S. Tarucha, *"A quantum-dot spin qubit with coherence limited by charge noise and fidelity higher than 99.9%,"* Nature Nanotechnology **13**, 102 (2018).

[5] W. Huang, C. H. Yang, K. W. Chan, T. Tanttu, B. Hensen, R. C. C. Leon, M. A. Fogarty, J. C. C. Hwang, F. E. Hudson, K. M. Itoh, A. Morello, A. Laucht, and A. S. Dzurak, *"Fidelity benchmarks for two-qubit gates in silicon,"* Nature **569**, 532 (2019).

[6] A. Noiri, K. Takeda, T. Nakajima, T. Kobayashi, A. Sammak, G. Scappucci, and S. Tarucha, *"Fast universal quantum gate above the fault-tolerance threshold in silicon,"* Nature **601**, 338 (2022).

[7] X. Xue, M. Russ, N. Samkharadze, B. Undseth, A. Sammak, G. Scappucci, and L. M. K. Vandersypen, *"Quantum logic with spin qubits crossing the surface code threshold,"* Nature **601**, 343 (2022).

[8] A. R. Mills, C. R. Guinn, M. J. Gullans, A. J. Sigillito, M. M. Feldman, E. Nielsen, and J. R. Petta, "Two-qubit silicon quantum processor with operation fidelity exceeding 99%," (2021), arXiv:2111.11937 [quant-ph].

[9] K. Takeda, A. Noiri, T. Nakajima, J. Yoneda, T. Kobayashi, and S. Tarucha, *"Quantum tomography of an entangled three-qubit state in silicon,"* Nature Nanotechnology **16**, 965 (2021).

[10] N. W. Hendrickx, W. I. L. Lawrie, M. Russ, F. van Riggelen, S. L. de Snoo, R. N. Schouten, A. Sammak, G. Scappucci, and M. Veldhorst, *"A four-qubit germanium quantum processor,"* Nature **591**, 580 (2021).

[11] R. Maurand, X. Jehl, D. Kotekar-Patil, A. Corna, H. Bohuslavskyi, R. Laviéville, L. Hutin, S. Barraud, M. Vinet, M. Sanquer, and S. De Franceschi, *"A CMOS silicon spin qubit,"* Nature Communications **7**, 13575 (2016).

[12] A. M. J. Zwerver, T. Krähenmann, T. F. Watson, L. Lampert, H. C. George, R. Pillarisetty, S. A. Bojarski, P. Amin, S. V. Amitonov, J. M. Boter, R. Caudillo, D. Corras-Serrano, J. P. Dehollain, G. Droulers, E. M. Henry, R. Kotlyar, M. Lodari, F. Luthi, D. J. Michalak, B. K. Mueller, S. Neyens, J. Roberts, N. Samkharadze, G. Zheng, O. K. Zietz, G. Scappucci, M. Veldhorst, L. M. K. Vandersypen, and J. S. Clarke, *"Qubits made by advanced semiconductor manufacturing,"* (2021), arXiv:2101.12650 [cond-mat.mes-hall].

[13] M. F. Gonzalez-Zalba, S. de Franceschi, E. Charbon, T. Meunier, M. Vinet, and A. S. Dzurak, *"Scaling silicon-based quantum computing using CMOS technology,"* Nature Electronics **4**, 872 (2021).

[14] E. Vahapoglu, J. P. Slack-Smith, R. C. C. Leon, W. H. Lim, F. E. Hudson, T. Day, T. Tanttu, C. H. Yang, A. Laucht, A. S. Dzurak, and J. J. Pla, *"Single-electron spin resonance in a nanoelectronic device using a global field,"* Science Advances **7**, eabg9158 (2021).

[15] L. C. Camenzind, S. Geyer, A. Fuhrer, R. J. Warburton, D. M. Zumbuhl, and A. V. Kuhlmann, "A spin qubit in a fin field-effect transistor," (2021), arXiv:2103.07369 [cond-mat.mes-hall].

[16] H. Watzinger, J. Kukucka, L. Vukusic, F. Gao, T. Wang, F. Schäffler, J.-J. Zhang, and G. Katsaros, *"A germanium hole spin qubit,"* Nature Communications **9**, 3902 (2018).

[17] D. Jirovec, A. Hofmann, A. Ballabio, P. M. Mutter, G. Tavani, M. Botifoll, A. Crippa, J. Kukucka, O. Sagi, F. Martins, J. Saez-Mollejo, I. Prieto, M. Borovkov, J. Arbiol, D. Chrastina, G. Isella, and G. Katsaros, *"A singlet-triplet hole spin qubit in planar Ge,"* Nature Materials **20**, 1106 (2021).

[18] F. N. M. Froning, L. C. Camenzind, O. A. H. van der Molen, A. Li, E. P. A. M. Bakkers, D. M. Zumbühl, and F. R. Braakman, *"Ultrafast hole spin qubit with gate-tunable spin–orbit switch functionality,"* Nature Nanotechnology **16**, 308 (2021).

[19] G. Scappucci, C. Kloeffel, F. A. Zwanenburg, D. Loss, M. Myronov, J.-J. Zhang, S. De Franceschi, G. Katsaros, and M. Veldhorst, *"The germanium quantum information route,"* Nature Reviews Materials **6**, 926 (2020).

[20] S. Bosco, B. Hetényi, and D. Loss, *"Hole spin qubits in* Si *finfets with fully tunable spin-orbit coupling and sweet spots for charge noise,"* PRX Quantum **2**, 010348 (2021).

[21] Z. Wang, E. Marcellina, A. R. Hamilton, J. H. Cullen, S. Rogge, J. Salfi, and D. Culcer, *"Optimal operation points for ultrafast, highly coherent Ge hole spin-orbit qubits,"* npj Quantum Information **7**, 54 (2021).

[22] A. Chatterjee, P. Stevenson, S. De Franceschi, A. Morello, N. P. de Leon, and F. Kuemmeth, *"Semiconductor qubits in practice,"* Nature Reviews Physics **3**, 157 (2021).

[23] B. Voisin, V.-H. Nguyen, J. Renard, X. Jehl, S. Barraud, F. Triozon, M. Vinet, I. Duchemin, Y.-M. Niquet, S. de Franceschi, and M. Sanquer, *"Few-electron edge-state quantum dots in a silicon nanowire field-effect transistor,"* Nano Letters **14**, 2094 (2014).

[24] B. Venitucci, L. Bourdet, D. Pouzada, and Y.-M. Niquet, *"Electrical manipulation of semiconductor spin qubits within the g-matrix formalism,"* Physical Review B **98**, 155319 (2018).

[25] C. Kloeffel, M. J. Rančić, and D. Loss, *"Direct rashba spin-orbit interaction in Si and Ge nanowires with different growth directions,"* Physical Review B **97**, 235422 (2018).

[26] V. P. Michal, B. Venitucci, and Y.-M. Niquet, *"Longitudinal and transverse electric field manipulation of hole spin-orbit qubits in one-dimensional channels,"* Physical Review B **103**, 045305 (2021).

[27] F. A. Zwanenburg, C. E. W. M. van Rijmenam, Y. Fang, C. M. Lieber, and L. P. Kouwenhoven, *"Spin states of the first four holes in a silicon nanowire quantum dot,"* Nano Letters **9**, 1071 (2009).

[28] N. Ares, V. N. Golovach, G. Katsaros, M. Stoffel, F. Fournel, L. I. Glazman, O. G. Schmidt, and S. De Franceschi, *"Nature of tunable hole g factors in quantum dots,"* Physical Review Letters **110**, 046602 (2013).

[29] A. Bogan, S. A. Studenikin, M. Korkusinski, G. C. Aers, L. Gaudreau, P. Zawadzki, A. S. Sachrajda, L. A. Tracy, J. L. Reno, and T. W. Hargett, *"Consequences of spin-orbit coupling at the single hole level: Spin-flip tunneling and the anisotropic g factor,"* Physical Review Letters **118**, 1 (2017).

[30] S. D. Liles, F. Martins, D. S. Miserev, A. A. Kiselev, I. D. Thorvaldson, M. J. Rendell, I. K. Jin, F. E. Hudson, M. Veldhorst, K. M. Itoh, O. P. Sushkov, T. D. Ladd, A. S. Dzurak, and A. R. Hamilton, *"Electrical control of the g tensor of the first hole in a silicon MOS quantum dot,"* Physical Review B **104**, 235303 (2021).

[31] T. Tanttu, B. Hensen, K. W. Chan, C. H. Yang, W. W. Huang, M. Fogarty, F. Hudson, K. Itoh, D. Culcer, A. Laucht, A. Morello, and A. Dzurak, *"Controlling spin-orbit interactions in silicon quantum dots using magnetic field direction,"* Physical Review X **9**, 021028 (2019).

[32] P. Stano and D. Loss, "Review of performance metrics of spin qubits in gated semiconducting nanostructures," (2021), arXiv:2107.06485 [cond-mat.mes-hall].

[33] E. Chanrion, D. J. Niegemann, B. Bertrand, C. Spence, B. Jadot, J. Li, P. A. Mortemousque, L. Hutin, R. Maurand, X. Jehl, M. Sanquer, S. De Franceschi, C. Bäuerle, F. Balestro, Y. M. Niquet, M. Vinet, T. Meunier, and M. Urdampilleta, *"Charge detection in an array of CMOS quantum dots,"* Physical Review Applied **14**, 1 (2020).

[34] F. Ansaloni, A. Chatterjee, H. Bohuslavskyi, B. Bertrand, L. Hutin, M. Vinet, and F. Kuemmeth, *"Single-electron operations in a foundry-fabricated array of quantum dots,"* Nature Communications **11**, 1 (2020).

[35] S. Schaal, I. Ahmed, J. A. Haigh, L. Hutin, B. Bertrand, S. Barraud, M. Vinet, C.-M. Lee, N. Stelmashenko, J. W. A. Robinson, J. Y. Qiu, S. Hacohen-Gourgy, I. Siddiqi, M. F. Gonzalez-Zalba, and J. J. L. Morton, *"Fast gate-based readout of silicon quantum dots using josephson parametric amplification,"* Physical Review Letters **124**, 067701 (2020).

[36] J. M. Elzerman, R. Hanson, L. H. Willems van Beveren, B. Witkamp, L. M. K. Vandersypen, and L. P. Kouwenhoven, *"Single-shot read-out of an individual electron spin in a quantum dot,"* Nature **430**, 431 (2004).

[37] B. Venitucci and Y.-M. Niquet, *"Simple model for electrical hole spin manipulation in semiconductor quantum dots: Impact of dot material and orientation,"* Physical Review B **99**, 115317 (2019).

[38] B. Martinez and Y.-M. Niquet, "Variability of electron and hole spin qubits due to interface roughness and charge traps," (2021), arXiv:2107.10902 [cond-mat.mes-hall].

[39] S.-D. Tzeng and S. Gwo, *"Charge trapping properties at silicon nitride/silicon oxide interface studied by variable-temperature electrostatic force microscopy,"* Journal of Applied Physics **100**, 023711 (2006).

[40] J. J. Pla, A. Bienfait, G. Pica, J. Mansir, F. A. Mohiyaddin, Z. Zeng, Y.-M. Niquet, A. Morello, T. Schenkel, J. J. L. Morton, and P. Bertet, *"Strain-induced spin-resonance shifts in silicon devices,"* Physical Review Applied **9**, 044014 (2018).

[41] B. Roche, E. Dupont-Ferrier, B. Voisin, M. Cobian, X. Jehl, R. Wacquez, M. Vinet, Y.-M. Niquet, and M. Sanquer, *"Detection of a large valley-orbit splitting in silicon with two-donor spectroscopy,"* Physical Review Letters **108**, 206812 (2012).

[42] A. Abragam and B. Bleaney, *Electron paramagnetic resonance of transition ions* (Clarendon Press, Oxford, 1970).

[43] G. Ithier, E. Collin, P. Joyez, P. J. Meeson, D. Vion, D. Esteve, F. Chiarello, A. Shnirman, Y. Makhlin, J. Schriefl, and G. Schön, *"Decoherence in a superconducting quantum bit circuit,"* Physical Review B **72**, 134519 (2005).

[44] E. Paladino, Y. Galperin, G. Falci, and B. Altshuler, *"1/$f$ noise: Implications for solid-state quantum information,"* Reviews of Modern Physics **86**, 361 (2014).

[45] H. Y. Carr and E. M. Purcell, *"Effects of diffusion on free precession in nuclear magnetic resonance experiments,"* Physical Review **94**, 630 (1954).

[46] S. Meiboom and D. Gill, *"Modified spin-echo method for measuring nuclear relaxation times,"* Review of Scientific Instruments **29**, 688 (1958).

[47] L. M. K. Vandersypen and I. L. Chuang, *"NMR techniques for quantum control and computation,"* Reviews of Modern Physics **76**, 1037 (2005).

[48] L. Cywiński, R. M. Lutchyn, C. P. Nave, and S. Das Sarma, *"How to enhance dephasing time in superconducting qubits,"* Physical Review B **77**, 174509 (2008).

[49] M. J. Biercuk, A. C. Doherty, and H. Uys, *"Dynamical decoupling sequence construction as a filter-design problem,"* Journal of Physics B: Atomic, Molecular and Optical Physics **44**, 154002 (2011).

[50] F. W. Olver, D. W. Lozier, R. F. Boisvert, and C. W. Clark, *NIST Handbook of Mathematical Functions*, 1st ed. (Cambridge University Press, USA, 2010).

[51] J. Medford, L. Cywiński, C. Barthel, C. M. Marcus, M. P. Hanson, and A. C. Gossard, *"Scaling of dynamical decoupling for spin qubits,"* Physical Review Letters **108**, 086802 (2012).

[52] Here we make use of two-sided power spectral densities, which are even with respect to the frequency.

[53] N. W. Hendrickx, D. P. Franke, A. Sammak, G. Scappucci, and M. Veldhorst, *"Fast two-qubit logic with holes in germanium,"* Nature **577**, 487 (2020).

[54] P. Machnikowski, K. Gawarecki, and L. Cywiński, *"Hyperfine interaction for holes in quantum dots: $k\cdot p$ model,"* Physical Review B **100**, 085305 (2019).

[55] S. Bosco and D. Loss, *"Fully tunable hyperfine interactions of hole spin qubits in Si and Ge quantum dots,"* Physical Review Letters **127**, 190501 (2021).

[56] I. A. Merkulov, A. L. Efros, and M. Rosen, *"Electron spin relaxation by nuclei in semiconductor quantum dots,"* Physical Review B **65**, 205309 (2002).

[57] J. Fischer, W. A. Coish, D. V. Bulaev, and D. Loss, *"Spin decoherence of a heavy hole coupled to nuclear spins in a quantum dot,"* Physical Review B **78**, 155329 (2008).

[58] C. Testelin, F. Bernardot, B. Eble, and M. Chamarro, *"Hole–spin dephasing time associated with hyperfine interaction in quantum dots,"* Physical Review B **79**, 195440 (2009).

[59] P. Philippopoulos, S. Chesi, and W. A. Coish, *"First-principles hyperfine tensors for electrons and holes in GaAs and silicon,"* Physical Review B **101**, 115302 (2020).